

NASA Contractor Report 198508

An Experiment on Losses in a Three-Port Wave Rotor

Jack Wilson
NYMA Inc.
Brook Park, Ohio

August 1997

Prepared for
Lewis Research Center
Under Contract NAS3-27186



National Aeronautics and
Space Administration

Trade names or manufacturers' names are used in this report for identification only. This usage does not constitute an official endorsement, either expressed or implied, by the National Aeronautics and Space Administration.

AN EXPERIMENT ON LOSSES IN A THREE-PORT WAVE ROTOR

Jack Wilson
NYMA, Inc.
Brook Park, Ohio 44142

Summary

Wave rotors used in a gas turbine topping cycle offer a potential route to higher specific power and lower specific fuel consumption. In order to exploit this potential properly, it is necessary to have some realistic means of calculating wave rotor performance, taking losses into account, so that wave rotors can be designed for good performance. This, in turn, requires a knowledge of the loss mechanisms. The experiment reported here was designed as a statistical experiment to identify the losses due to finite passage opening time, boundary layers, and leakage. On analyzing the data, incidence loss was also determined to be an important loss. For simplicity, the experiment used a three-port, flow divider, wave cycle, but the results are applicable to other cycles. A 12-in.-diameter rotor was used with two different lengths, 9 and 18 in., and two different passage widths, 0.25 and 0.54 in., in order to vary the boundary layer thicknesses and the opening time. To vary leakage, moveable end walls were provided so that the rotor to end-wall gap could be adjusted. The experiment is described and the results are presented together with a parametric fit to the data. The fit shows that there will be an optimum passage width for a given wave rotor since, as the passage width increases boundary layer losses decrease, but opening-time losses increase and vice-versa. Leakage losses can be made small at reasonable gap sizes. Inlet ports should be designed to minimize incidence losses.

Introduction

The performance of gas turbine engines can be improved if the temperature after combustion can be raised. This is difficult to do because the turbine inlet temperature is limited by material considerations (Peacock and Sadler, 1992). Increased performance can be achieved if the pressure entering the turbine can be increased. If the engine is already at the optimum compression ratio for that turbine inlet temperature, increasing the compression ratio in order to increase the turbine inlet pressure will not result in improved performance. Increased performance will result if the combustion step can be config-

ured so as to result in a pressure gain, rather than a pressure loss. Two techniques for achieving this are unsteady combustion (Kentfield, 1995), and the use of a wave rotor topping cycle (Meyer, 1947, Zauner, et al., 1993, and Kentfield, 1995). Because unsteady combustion currently shows only modest pressure gains, the wave rotor approach seems preferable. Calculations show that increases of 20 percent in specific power, and reductions of 18 percent in specific fuel consumption are possible by using a wave rotor topping cycle (Wilson and Paxson, 1996, and Welch, Jones, and Paxson, 1997).

Wave rotors are devices that use unsteady waves rather than turbomachinery to compress and expand gas streams. The rotor itself has a set of passages on its periphery. In the present experiment, which was designed for no exchange of shaft work, the passages are straight and aligned axially. As the rotor rotates, these passages are alternately exposed to ports at differing pressures. Typically, at the exhaust or low-pressure port, the passage contains gas at some higher pressure just before the passage rotates into juxtaposition with the port. Exposure to the low port pressure causes an expansion wave to propagate into the passage. Later in the cycle, the passage, now at lower pressure, will be opened to the inlet port where the gas is at higher pressure, thereby causing a shock wave to be propagated into the passage, increasing the stagnation pressure of the gas. The exact sequence of waves will depend on the cycle employed. Several different cycles are possible, each serving a different function. Examples are three-port cycles used as flow dividers or equalizers (Kentfield, 1969), four-port cycles used for superchargers (Jenny and Zumstein, 1982), topping cycles for gas turbine engines (Meyer, 1947, Zauner, et al., 1993), a wave superheater wind-tunnel (Weatherston, et al., 1959), and five and nine port cycles again intended for use as topping cycles (Thayer, et al., 1981). In addition, wave engines for generating shaft power have been developed (Pearson, 1985, and Weber, 1995). However, all the cycles have common features. For example, all cycles employ an expansion wave and expanding through too large a pressure ratio leads to losses for any cycle. Obviously, for maximum output, whatever the application, the efficiency of the wave rotor should be as high as possible, i.e., the losses should be minimized. In order to do this, it is necessary to know the source

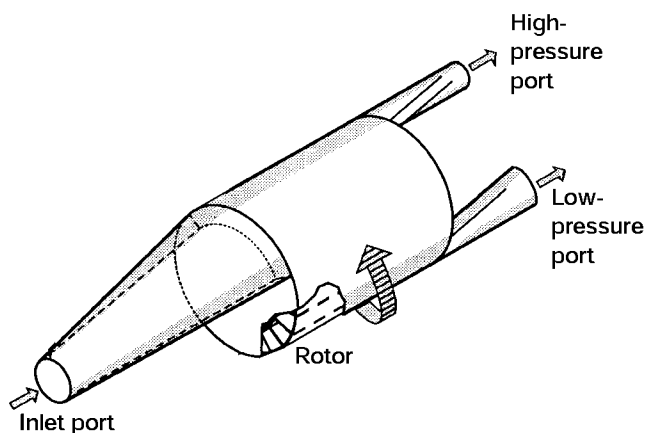


Figure 1.—The flow divider apparatus.

of the losses and their dependence on controlling parameters. This study is aimed at assessing experimentally the magnitude of various wave rotor losses as a function of the parameters which affect them. This will be achieved by measuring the performance of a wave rotor as various geometrical parameters (passage width, rotor length, and rotor-casing clearance) are varied. The losses are not specific to one cycle and so any convenient cycle can be used for this study. For simplicity, the three-port flow divider cycle was chosen. In the flow divider, a single inlet flow is split into two outlet flows, one at higher stagnation pressure than the inlet flow, and the other at lower stagnation pressure than the inlet flow. No heat is added so the apparatus is relatively simple (fig. 1).

In order to make an experimental study of losses, a wave rotor has been built at NASA Lewis Research Center, operating on the three-port flow divider cycle. This report contains a brief statement of the philosophy of the experiment, a description of the experiment, a discussion of the loss mechanisms, and a summary of the measurements made. Results are presented showing that reduction of the rotor-to-wall clearance gap leads to a large improvement in performance, and that friction, incidence loss, and opening-time effects also play an important role in the performance.

Additional tests to examine the effects of brush seals, rounding the leading edge of the inlet port, and pressure variation are also reported.

Symbols

A area of inlet port

a speed of sound

B width of a passage on the rotor

b_o, b_p, b_{ii} constants defined in equation (35)

C_p specific heat at constant pressure

c incidence coefficient

D rotor diameter

D_h hydraulic diameter of passages

$D(x)$ drag on a plate of length x

F dimensionless friction parameter, defined in equations (3), (5), and (7)

f constant defined in equation (21)

G, G_p, G_w leakage parameter, defined in equations (28) to (34)

H height of a passage on the rotor

HP power put into the gas by the rotor

i angle of incidence of entering air in the rotor reference frame

K coefficient of incidence loss

L length of the rotor

M_j Mach number in region j

m_i $\rho_i V_i \cos \alpha_i$; mass flow per unit area at station i in inlet port

n potential number of cycles on the rotor

P_j absolute stagnation pressure in region j

Pr_j relative stagnation pressure in region j

R radius of the rounding on the leading edge of the inlet port

T_j absolute stagnation temperature in region j

Tr_j relative stagnation temperature in region j

t time

U circumferential velocity of the rotor at the average radius of the passages

V_j absolute velocity in region j

W_j	relative velocity in region j
x	distance along a passage
α	angle of flow in inlet duct
β	ratio of mass flow in high-pressure port to total mass flow
γ	ratio of specific heats
δ	end-wall to rotor gap spacing
δ_p	end-wall to rotor gap spacing at a port
δ_w	end-wall to rotor gap spacing away from a port
$\delta_2(x)$	boundary layer momentum thickness at x
ε	expansion ratio—ratio of the pressure in the low-pressure port to the pressure in a passage just before reaching the low-pressure port
η	efficiency
θ_p	angular extent of low-pressure port
$\theta_{w_{in}}$	angular extent of low-pressure region at inlet end wall
$\theta_{w_{out}}$	angular extent of low-pressure region at exit end wall
θ_w	$\theta_{w_{in}} + \theta_{w_{out}}$
ν	kinematic viscosity
ρ	gas density
τ	dimensionless opening time, defined in eq. (2)
ω	rate of rotation of the rotor
Subscripts	
cav	cavity surrounding the rotor into and from which leakage occurs
j	general subscript for any of the three subscripts below:
hi	high-pressure port
in	inlet port
lo	low-pressure port

L	laminar
pas	passage immediately before opening to the low-pressure port
T	turbulent
Superscripts	
fpc	at exit of flat plate compressor with losses
ll	lossless value at exit of flat plate compressor
'	isentropic value

The Flow Divider Cycle

The performance of a flow divider at optimum speed is conveniently indicated on a plot of the ratio of high stagnation pressure to inlet stagnation pressure versus the ratio of low stagnation pressure to inlet stagnation pressure, with the mass flow ratio β as a parameter (Kentfield, 1969). An upper limit to the performance of the flow divider can be calculated very simply by using what is called the acoustic approximation. In this approximation, the following assumptions are made about the flow:

1. Flow conditions are constant within each region; regions are separated by waves.
2. Waves are not reflected at ports.
3. Waves travel at a single speed, which is the average of the wave propagation speeds on either side of the wave, and hence, do not spread.
4. No change in entropy occurs across the waves.

The results of this calculation are shown in figure 2(a). This performance, which is called the isentropic performance, is significantly higher than anything that can be achieved in practice, but it does illustrate the features of flow divider performance, i.e., that a large ratio of high pressure to inlet pressure is only achieved at a low value of β . The dotted line terminating the curves of constant mass ratio β at the upper left corresponds to an inlet Mach number of unity. In this approximation, the curves of constant β are concave upwards, and maximum performance (i.e., the largest high-pressure ratio) will be achieved at an inlet Mach number of unity.

A more accurate calculation can be made by using the method of characteristics to evaluate the expansion out of the passages into the low-pressure port, and by including shock waves in the compression portion of the calculation. This will be called the ideal cycle. In this cycle, the velocity in the low-pressure port will be uniform until the arrival of the reflected expansion wave, then decreasing to zero at port closing. This will cause a total pressure loss as the flow mixes to a uniform

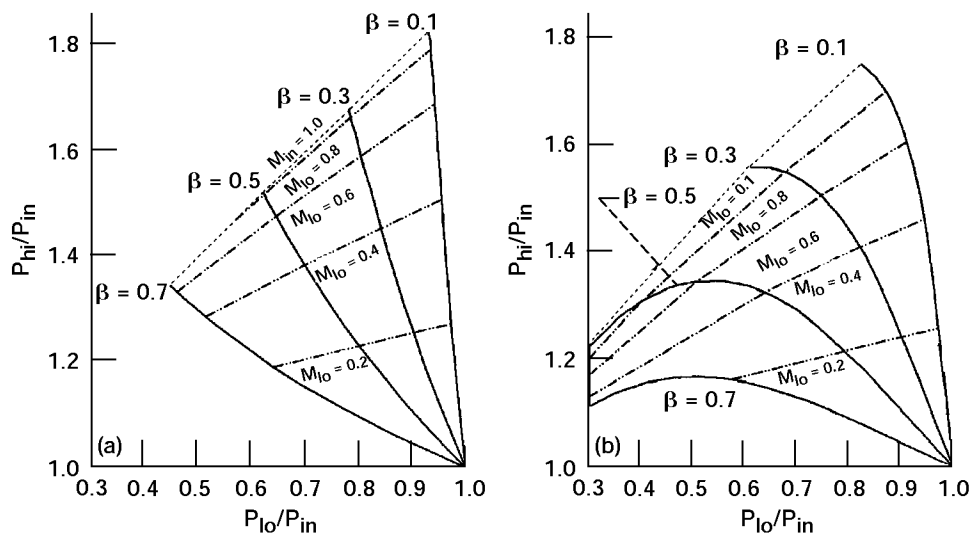


Figure 2.—Performance of a three-port flow divider calculated using the (a) isentropic and (b) ideal cycles.

velocity. The resulting flow divider performance is shown in figure 2(b). Now the curves of constant β are concave downwards, and the maximum performance (whether defined as pressure rise or efficiency) occurs for an inlet Mach number less than unity. A further important difference is where choking occurs. For the isentropic cycle, the inlet Mach number is greater than either of the outlet Mach numbers, and choking would occur at the inlet. In the ideal cycle, for values of β of 0.5 and less, reducing the low pressure leads to a Mach number of unity in the low-pressure port while the inlet port is still subsonic. In other words, choking occurs at the low-pressure port, not the inlet port. Although the ideal performance contains wave losses which are inherent in any real cycle, and so is a better approximation than the isentropic calculation, it cannot be achieved in practice since there is an inherent assumption that the passages open to the ports instantaneously (zero opening time), nor is any loss due to boundary layers included. These conditions are obviously not attainable.

The isentropic assumption is only valid for weak waves, which is the case for the lower right hand region of figure 2, where pressure ratios are close to unity. Comparison of figures 2(a) and (b) shows that the isentropic calculation works reasonably well for outlet Mach numbers M_{lo} less than about 0.3. The experiments of Kentfield (1969) were entirely within this range, and his curves did not display a pressure ratio maximum. For topping-cycle application, admittedly with a different cycle, the exit pressure ratio should be as large as possible. Consequently, one consideration in the present experiment was to operate the wave rotor under conditions for which the acoustic approximation would not be valid, and observe whether there is indeed a maximum pressure ratio. Consequently, a design expansion ratio of 0.33, at $\beta = 0.37$ was chosen, corresponding to a Mach number of the initial

expanded flow of 0.85 (before the arrival of the reflected expansion wave). The expansion ratio is the ratio of the static pressure in the low-pressure port to the pressure in a rotor passage just before it is opened to the low-pressure port. This ratio determines the Mach number of the flow in the low-pressure port. For an expansion ratio of 0.33, the expansion wave exhibits significant spreading, as can be seen in the x-t diagram of the cycle shown in figure 3, as calculated using characteristics.

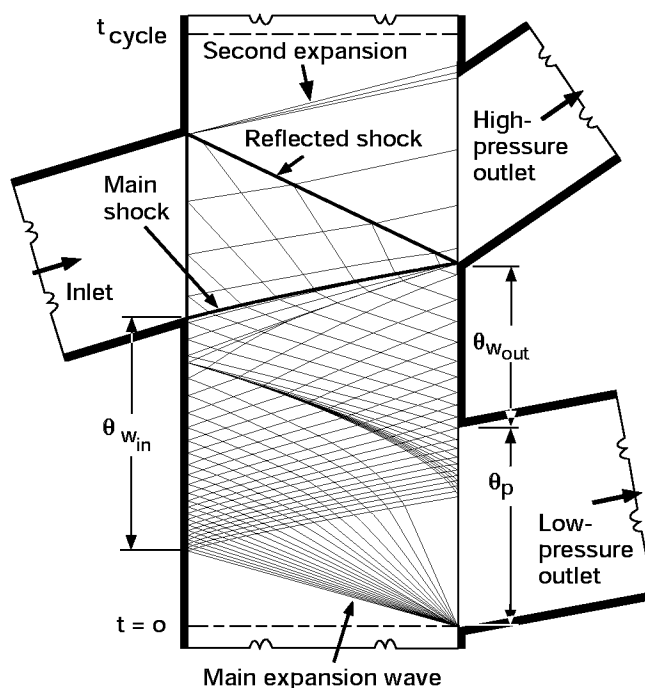


Figure 3.— Characteristics calculation of the flow divider cycle for $\epsilon = 0.33$.

The efficiency of a flow divider has been defined by Kentfield (1969) as the product of compression and expansion efficiencies

$$\eta = \left[\left(\frac{T'_{hi}/T_{in} - 1}{T_{hi}/T_{in} - 1} \right) \right] \cdot \left[\left(\frac{1 - T_{lo}/T_{in}}{1 - T'_{lo}/T_{in}} \right) \right]$$

$$= \frac{\beta}{(1-\beta)} \left[\frac{(P_{hi}/P_{in})^{(\gamma-1)/\gamma} - 1}{1 - (P_{lo}/P_{in})^{(\gamma-1)/\gamma}} \right] \quad (1)$$

The isentropic performance can be obtained from this formula by inserting $\eta = 1$.

Loss Mechanisms

Although several wave rotors have been built in the past, only two studies of losses appear to have been reported, namely theoretical estimates of losses by Hoerler (1969) for the Comprex[®], and by Kentfield (1969) for the flow divider. However, Thayer, et al. (1981) observed an increase in efficiency on reducing the rotor to end-wall gap, which would have reduced leakage losses. Kentfield (1969) gives the following losses as being in order of decreasing importance:

1. Basic wave effects
2. Cell width, i.e., opening time effects
3. Wall friction, passage entry, and exit losses
4. Leakage

Hoerler calculated losses for the rotor itself as percentage losses in efficiency for an experimental Comprex and also for a hypothetical optimized Comprex. The results are given in table I. In addition, he calculated losses for ducts and stators external to the rotor. Hoerler stated that leakage can dominate all other rotor losses, particularly for small machines, which is

just the opposite of the conclusions by Kentfield (1969). This disagreement reflects the different geometries of the two machines considered, as will be explained in the Leakage section.

It will be assumed that the friction, opening-time, and leakage losses will scale with one predominant parameter for each loss. The derivation of the parameter for each of these losses plus the estimation of other losses will be outlined below.

Basic Wave Effects

Basic wave effects are the losses that result from shock waves and the spreading of expansion waves. Shock and expansion waves cause the difference in performance between the ideal and the isentropic cycles. A real cycle can have shock waves instead of compression waves. There is a loss of stagnation pressure across a shock wave, leading to a reduction in performance. Expansion waves spread in space as they propagate, resulting in nonuniform velocities in the exit ports. Mixing of the nonuniform velocity distribution to form a uniform distribution causes a stagnation pressure loss. These losses are unavoidable in a real device. Moreover, they are quite large at low values of expansion ratio, as can be seen by the differences between the performance shown in figures 2(a) and (b). The losses caused by these effects depend on β and ϵ , and are readily calculable if the timing is correct, that is, if the ports open and close at the appropriate times as determined by the arrival or launching of waves. For maximum performance, the timing will be different for each value of β and ϵ considered. An actual device will usually have timing fixed for one set of conditions, and operation off-design will create extra waves, causing additional losses. This situation can be handled computationally using CFD codes for wave rotor cycles (e.g., Paxson, 1995). Lines of equal pressure, density, and velocity calculated for on-design conditions with the one-dimensional CFD code of Paxson (1995) are shown in figure 4. The agreement in the position of the waves with the characteristics calculation is very good. The ideal cycle performance can not be measured directly in an experiment. It can be determined from experimental results by measuring performance as a function of the other losses and extrapolating them to zero.

Finite Passage Opening Time

Since the passages have a finite width, there is a finite time taken for a passage to rotate past the leading or trailing edge of a port and become fully open or closed. In the case of an inlet port for which instantaneous opening of the passage would cause a shock wave to propagate down the passage, a finite opening time will result in a compression wave, which will steepen into a shock as it travels down the passage. The degree to which it steepens depends on the ratio of the opening time to the time taken by the wave to travel the length of the passage. Thus the relevant nondimensional parameter is

TABLE I.—LOSS OF EFFICIENCY IN A COMPREX[®]

Source of Loss	Loss in experimental Comprex, percent	Loss in optimized Comprex, percent
Shocks and Fans	4.5	3.3
Passage opening/closing	4.1	4.2
Friction (turbulent)	7.2	2.1
Heat transfer	3.3	2.1
Rotational velocity	4.2	2.0
Leakage	10.1	1.1
Mechanical	2.3	0.1
Interface mixing	0	0
Total	35.7	14.9

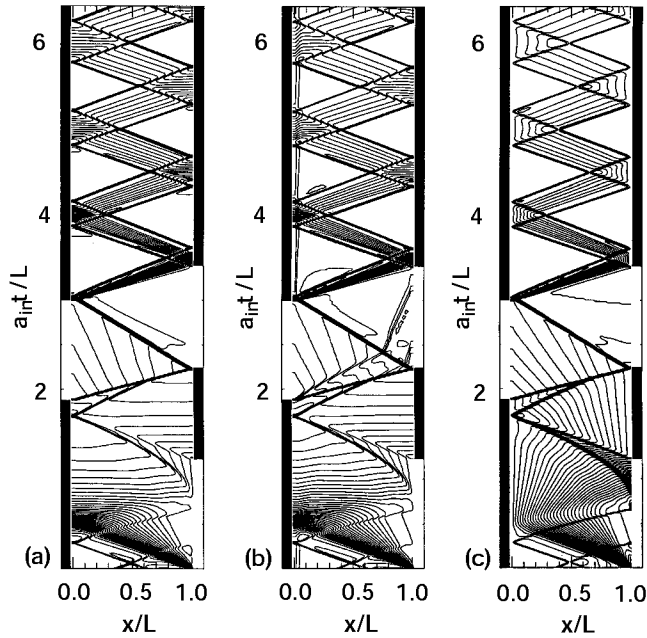


Figure 4.—Lines of constant (a) pressure, (b) density, and (c) velocity in the flow divider, as calculated for on-design flow using the CFD model of Paxson (1995).

$$\tau = \frac{\text{Passage Opening Time}}{\text{Wave Travel Time}} = \left(\frac{B}{U} \right) \left(\frac{a}{L} \right) \quad (2)$$

The speed of sound, a , will vary depending on which region of the cycle is being considered. For simplicity of definition, the inlet stagnation value will be used. Note that for any particular cycle, the rotor velocity U will be inversely proportional to the axial length of the passage L , and hence τ is determined mainly by the value of the passage width B . In addition to the effect on wave steepening, which may be advantageous, finite opening time will result in deleterious throttling losses when the passage is partially open. Further, finite opening time will create at least a gradual rise in velocity at the outlet ports, and finite closing time will create a gradual reduction in velocity at the outlet ports. In fact, jets may be created giving a greater flow disturbance. The resulting nonuniform velocity distribution will result in a drop in stagnation pressure when it is mixed out to a uniform value downstream. Clearly, this loss will increase as τ increases.

Boundary Layers

Although the rotor passages are long and slender, their maximum length to width ratio is less than the entrance length

for pipes. Thus, the flow can be considered to have a boundary layer. This is confirmed by measurements of the radial velocity distribution in the high-pressure port, showing a uniform velocity over the central 70 percent of the passage, and also by two-dimensional calculations of the flow in the entrance and high-pressure ports of the experimental geometry (Welch and Chima, 1994), which show a relatively small boundary layer. The flow in a passage open to the low-pressure port can be thought of as flow over a flat plate, with the leading edge of the “plate” being the location of the leading edge of the expansion wave. A friction parameter can then be defined as the ratio of the drag force due to the flat plate to the product of dynamic pressure and flow area, i.e.,

$$F = D(x) / \left(\frac{1}{2} \rho W^2 B H \right) \quad (3)$$

The drag is related to the boundary layer momentum thickness at the end of the passage (Schlichting, 1979). Hoerler (1969) assumed the boundary layer was turbulent. With this assumption, the boundary layer momentum thickness is given by (Schlichting, 1979)

$$\delta_2(x) = 0.036x(Wx/v)^{-0.2} \quad (4)$$

The length of the boundary layer varies linearly with time as the expansion moves into the passage. By averaging over the time that the port is open, the friction parameter becomes

$$F_T = 0.32 \frac{L}{D_h} \left[\frac{LW}{v} \right]^{-0.2} \quad (5)$$

For a laminar boundary layer, the momentum thickness is given by (Schlichting, 1979)

$$\delta_2(x) = 0.67x(Wx/v)^{-0.5} \quad (6)$$

which leads to a laminar friction factor of

$$F_L = 7.2 \frac{L}{D_h} \left[\frac{LW}{v} \right]^{-0.5} \quad (7)$$

These friction parameters will be taken as representative of the effect of friction on the cycle as a whole. The dominant factor in either friction parameter is L/D_h .

Heat Transfer

Since it was not possible to measure heat transfer due to the lack of a sensor with a sufficiently rapid response rate, there seemed little point in making a separate assessment for heat

transfer. It will depend on the same parameter as friction, so the two losses were simply incorporated together as one loss. In any case, heat transfer is very low in a flow divider cycle.

Rotational Velocity Effect

The wave action takes place entirely within the rotor, producing changes of pressure in the relative frame. However, the actual performance of a device is measured in the absolute frame, and will be affected by the rotor rotational speed. The experiments were run at three different rotational speeds, and so should be compared in the relative frame to remove the effect of the differing rotational speeds. Also, the ideal performance, as given above, is in the relative frame (since no correction for rotation was made, which is equivalent to assuming that the rotational velocity is zero). Thus it is necessary to correct the observed absolute results to the relative frame.

The ratio of relative to absolute stagnation pressure is

$$\frac{Pr_j}{P_j} = \left[\frac{Tr_j}{T_j} \right]^{\gamma/(\gamma-1)} \quad (8)$$

If no work is done on the gas, the relative temperatures will be related to the absolute temperatures by

$$Tr_j = T_j - U^2/2C_p \quad (9)$$

The absolute efficiency, calculated by inserting absolute values of stagnation pressure into equation (1), will be less than the relative efficiency calculated by using relative stagnation pressures in equation (1). Thus, this effect is equivalent to a loss. For the flow divider (though not necessarily for other cycles), this effect is small. Even at the highest rotational speed used in the experiment, the drop in efficiency is only 1 percent.

Flat Plate Compressor Effect

If the inlet duct is at the correct angle, and if the flow angle α is equal to the duct angle everywhere in the port, then the inlet flow will enter the passages smoothly at zero angle of incidence in the relative frame, $i = 0$ (fig. 5). For this to be the case, the flow angle must satisfy the relation

$$\sin(\alpha) = U/V_{in} \quad (10)$$

This will only occur if the flow velocity is uniform and the duct is designed correctly.

Off-design, the flow will be at a finite angle of incidence i to the passage side walls, and work will be done on the air if i is negative or extracted from it if i is positive. Thus, the rotor acts as a flat plate compressor. The work done on the gas will result in a stagnation temperature rise ΔT ,

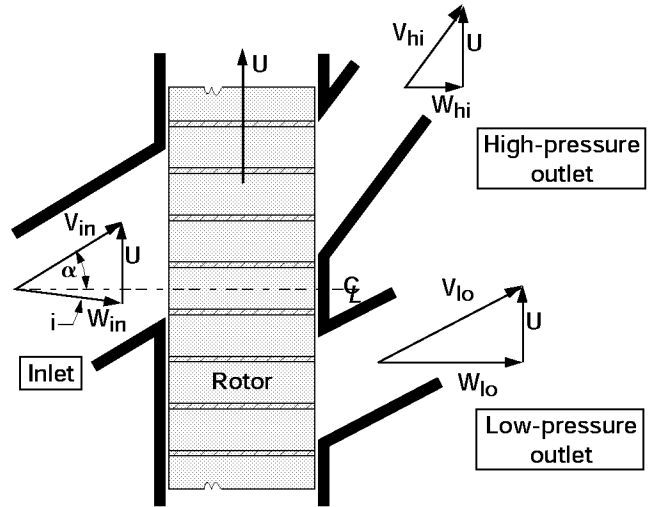


Figure 5.—Velocity diagrams for the flow divider.

$$\Delta T = \beta T_{hi} + (1 - \beta) T_{lo} - T_{in} \quad (11)$$

which can be calculated from the Euler equation for turbomachinery:

$$C_p \Delta T = U(U - V_{in} \sin(\alpha)) \quad (12)$$

In reality, both the velocity V_{in} and the flow angle α vary across the inlet port, and the work done must be evaluated by integration. Thus, if the inlet port is divided into 11 stations, the power put into the air will be

$$\begin{aligned} HP = 0.339A & \left[0.5 m_o U(U - V_o \sin \alpha_o) \right. \\ & + 0.5 m_{10} U(U - V_{10} \sin \alpha_{10}) \\ & \left. + \sum_{i=1}^9 m_i (U - V_i \sin \alpha_i) \right] / 10C_p \quad (13) \end{aligned}$$

The factor 0.339 is the specific heat of air in units of hp/lb/sec°R.

This calculation provides the work put into the gas by the rotor, but does not give values for pressure. With work input, the relative inlet stagnation temperature (at any station) is given by

$$\begin{aligned} Tr_{in} &= T_{in} - U^2/2C_p + U(U - V_{in} \sin \alpha)/C_p \\ &= T_{in} + (U^2/2 - UV_{in} \sin \alpha)/C_p \quad (14) \end{aligned}$$

A lossless flat plate compressor would generate a relative stagnation pressure of

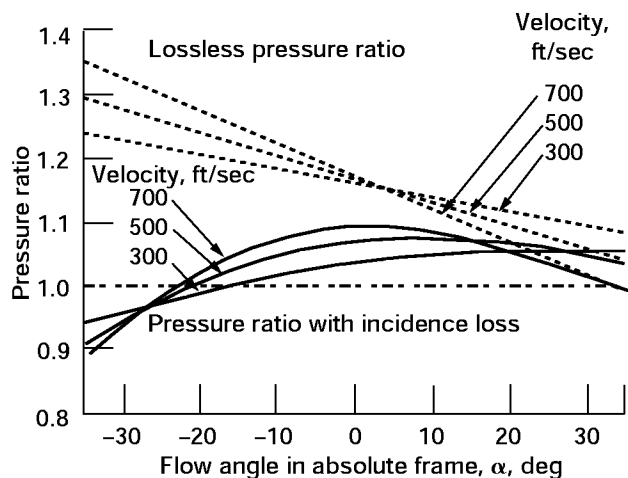


Figure 6.—Ratios of relative stagnation pressure (both lossless and with incidence losses) generated by the flat plate compressor to the relative stagnation pressure with no work for $U = 388$ ft/sec.

$$Pr_{in}^{II} = P_{in} (Tr_{in}/T_{in})^{\gamma/(\gamma-1)} \quad (15)$$

The lossless relative stagnation pressure divided by the relative stagnation pressure for no work (eq. (9)) is shown in figure 6 as a function of inlet angle for three different absolute velocities at a circumferential velocity of 388 ft/sec, the maximum value used in the experiment. For all flow angles less than 34° , this ratio is greater than unity, showing that work is being done on the air.

Keller (1984) has shown that the leading edge of a wave rotor inlet port should be rounded to minimize losses due to vortex shedding. Keller gives a criterion for the radius of the rounding

$$R \geq BU/V_{in} \quad (16)$$

In order to ensure that this criterion was well satisfied in the present experiment, a large radius (1.62 in.) was chosen, but the circle was truncated. This geometry is sketched in figure 7. Unfortunately, this rounding was too large, as it affected the inlet flow field causing a large fraction of the flow to enter the rotor at an angle less than that for zero relative incidence angle resulting in work being done on the air by the rotor. Air hitting a row of airfoils at an angle of incidence will suffer a loss of stagnation pressure called incidence loss. Data on loss of kinetic energy due to incidence has been given by Emmert (1950) for both sharp-edged blades and round-nosed blades (without defining what constitutes sharp and round). Emmert defined an incidence coefficient c such that the kinetic energy at incidence is the product of c and the kinetic energy at zero incidence. Roelke (1994) stated that the dependence of incidence loss of kinetic energy on incidence angle i for a turbine is given by

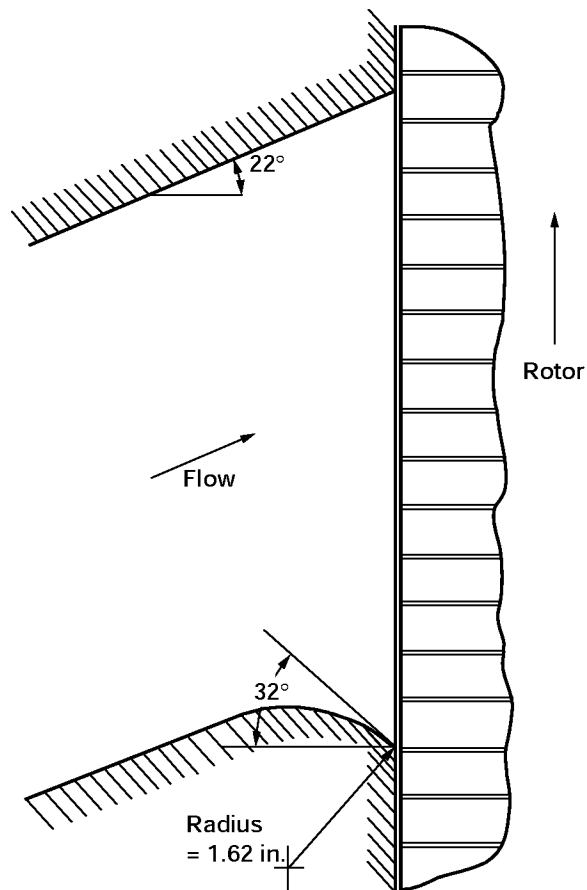


Figure 7.—The geometry of the inlet port for a duct angle of 22° showing the leading edge rounding.

$$c = \cos^2(i) \quad (17)$$

and points out that this is equivalent to losing the component of kinetic energy normal to the blade. The loss of stagnation pressure due to incidence loss can be defined as

$$\Delta P = K \frac{1}{2} \rho W_{in}^2 \quad (18)$$

from which it follows that for incompressible flow

$$K = (1 - c) \quad (19)$$

and using equation (17) for the dependence of c on i

$$K = \sin^2(i) \quad (20)$$

In figure 8, the Emmert data converted to K using equation (19) has been plotted against incidence angle. Also shown is the curve given by equation (20) and two curves corresponding to

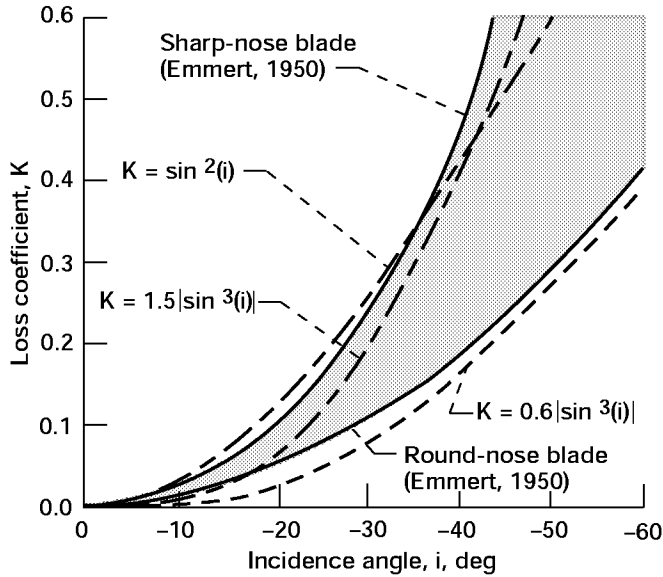


Figure 8.—The data of Emmert (1950) for incidence loss coefficient K versus incidence angle (shaded region) together with several fits to the data.

$$K = f |\sin^3(i)| \quad (21)$$

The curve with $f = 0.6$ is a good fit to the round-nose blade data, and the curve with $f = 1.5$ is a reasonable fit to the sharp-nose blade data. Particularly at large incidences, where the losses are more significant, the shape of equation (21) approximates the data better than does equation (20). Consequently, equation (21) was selected to correct the data for incidence losses. However, the value of f is not yet determined. Depending on whether the leading edge of the passages is sharp or round, the value could apparently be between 0.6 and 1.5.

The loss coefficient is dependent on Mach number, as well as on incidence angle. Data on loss coefficients for cascades of four different airfoils at a variety of Mach numbers has been given by Lieblein (1965). The data of figure 13(d) of Lieblein, which is for a sharp-edged airfoil, can be fit quite well using the expression

$$K = K_0 + f |\sin^3(i)| \quad (22)$$

where f increases with Mach number from a value of 11 at a Mach number of 0.4 to a value of 170 at a Mach number of 0.8. In addition to varying with Mach number, values of loss coefficient can depend on Reynolds number and solidity. In the present experiment, the Mach number varies between about 0.2 and 0.9. Thus, the value of f could be much larger than the values which fitted the data of Emmert. A priori, there is no obvious value of f to use. Instead, values of f were chosen, the data were corrected with this value and then extrapolated to obtain an experimental value for the efficiency with no friction, zero opening time, and no leakage, that is, the maximum

efficiency. This maximum efficiency is equal to the ideal efficiency at the design condition $\varepsilon = 0.33$. For off-design conditions, the ideal efficiency requires the port timing to be changed for each value of ε . The term maximum efficiency will be used here to mean the efficiency with $\tau = F = G_P = G_W = 0$, but with the fixed experimental timing. The value of f was altered until the experimental value of maximum efficiency agreed with the maximum efficiency calculated using the 1-D CFD Code of Paxson (1995). In other words, the experiment, together with the 1-D code, was used to determine a value of f .

With a value of f assumed, the relative stagnation pressure produced by the flat plate compressor is

$$Pr_{in}^{fpc} = Pr_{in}^{ll} - \frac{1}{2} \rho_{in} W_{in}^2 f |\sin^3(i)| \quad (23)$$

The ratio of relative stagnation pressure from equation (23) divided by the relative stagnation pressure for no work (eq. (9)) is also shown in figure 6 for a value of $f = 2$. The work input into the air increases as the flow angle decreases as shown by the increase in the lossless pressure ratio given in figure 6. With losses, for flow angles less than about -15° , depending on velocity, the relative stagnation pressure is less than it would be with no work input. The incidence losses have caused a pressure loss greater than the pressure increase due to work input.

Since the flow angle and velocity vary across the inlet port, the relative stagnation pressure will also vary across the inlet port. A single value is required for input into the efficiency equation and is obtained by averaging the relative stagnation pressures calculated at the same 11 stations across the port used in calculating the work input.

$$Pr_{in}^{fpc} = \left[Pr_{in}^{fpc}(1) + 4 \sum_{j=0}^4 Pr_{in}^{fpc}(2j+1) + 2 \sum_{j=0}^4 Pr_{in}^{fpc}(2j) + Pr_{in}^{fpc}(10) \right] / 30 \quad (24)$$

Leakage

Leakage can take place radially from the passage to the casing if the passage is at high pressure, or from the casing to the passage if the passage is at low pressure. The result will be a “short-circuiting” from high pressure to low pressure leading to reduced performance. In addition, circumferential leakage is possible from passage to passage. The pressure difference driving circumferential leakage is small except at those tangential positions where a wave has reached the end of a passage. Since these regions are of limited extent, circumferential leakage is likely to be small. For radial leakage, the rate of mass leakage will be proportional to the area available for leakage

which is $2\delta B$ at each end of a passage. The leakage will be into the passage while it is in a region of low pressure. From figure 3, the low-pressure region on the inlet side extends over an angle $\theta_{w_{in}}$, and on the outlet side, the low-pressure region is the low-pressure port, of extent θ_p , and the region between the low-pressure port and the high-pressure port, of extent $\theta_{w_{out}}$. Thus the time spent at low pressure is

$$t = \theta_{w_{in}} / \omega \quad (25)$$

at the inlet side of the wave rotor and

$$t = \theta_p / \omega + \theta_{w_{out}} / \omega \quad (26)$$

at the outlet side of the wave rotor. The amount of mass leaking into a passage in one cycle will be

$$\text{mass} \sim \rho_{cav} 2B (\delta_w \theta_{w_{in}} + \delta_p \theta_p + \delta_w \theta_{w_{out}}) / \omega \quad (27)$$

Defining a leakage parameter as the ratio of the mass leakage to the mass in a passage before it reaches the low-pressure port, that is, ρ_{pas} BHL, the leakage parameter becomes, if ρ_{pas} is assumed equal to ρ_{cav}

$$G \sim 2(\delta_p \theta_p + \delta_w \theta_w) \omega HL \quad (28)$$

For operation of a specific wave rotor, ωL is a constant. For convenience, relative values of θ_p , and θ_w , can be used such that

$$\theta_p + \theta_w = 2 \quad (29)$$

and the proportionality constant chosen so that the leakage parameter is defined as

$$G = (\delta_p \theta_p + \delta_w \theta_w) / H \quad (30)$$

Then if the leakage gaps are equal, i.e., $\delta_p = \delta_w = \delta$, this reduces to

$$G = 2\delta/H \quad (31)$$

Based on this derivation, one would expect that the leakage in the Comprax studied by Hoerler (1969) would be similar to that in the experiments of Kentfield (1969), since the ratio $2\delta/H$ was virtually the same for both devices, but Hoerler claimed leakage was important, whereas Kentfield said that it was not. However, the two devices operated on quite different cycles, and whereas the experiment of Kentfield used a similar cycle to that of the present experiment, the Comprax cycle was

different. In the Comprax, which used a four-port cycle, the inlet port and exhaust port were at approximately the same pressure, which was significantly lower than the two high-pressure ports. Therefore, the cavity was likely to be at some intermediate pressure. This means that the assumption above that $\rho_{cav} = \rho_{pas}$ is probably not correct for the Comprax, and also there would be leakage into the inlet port. Both of these effects would lead to more leakage. An additional difference was the relative extent of the low-pressure regions, with more of it in a port region for the Comprax. Thus, it seemed important to ascertain in the present experiment whether leakage at a wall is more or less important than leakage at a port. In order to do this, the wall gap and port gap were varied independently. Thus separate port and wall leakage parameters were defined, i.e.,

$$G_p = \delta_p \theta_p / H \quad (32)$$

$$G_w = \delta_w \theta_w / H \quad (33)$$

Relative values of $\theta_p = 0.71$ and $\theta_w = 1.29$ were used so that when the wall and port gaps are equal, the total leakage parameter

$$G = G_p + G_w = (0.71\delta + 1.29\delta)/H = 2\delta/H \quad (34)$$

is in agreement with equation (31).

Entrance and Exit Losses

The wall between the passages has a finite thickness ($= 0.040$ in.). There is consequently an area change between flow in the ducts and flow in the passages. The squared ends of the walls will present an obstruction to the flow on entering, and a drag on leaving, leading to stagnation pressure losses. This effect was calculated by assuming the leading edge is at the entering stagnation pressure, and the trailing edge is at the downstream static pressure. The resulting force on the flow is included in the momentum equation, which is then solved with the continuity and energy equations to give the mixed-out downstream stagnation pressure. The losses in stagnation pressure are less than 2 percent for the narrow passages, and less than 1 percent for the wide passages. A plot of the calculated entrance losses, expressed as the ratio of stagnation pressure loss to initial stagnation pressure is given in figure 9, and a plot of the exit losses is given in figure 10.

Summary of Losses

The losses described above are summarized in figure 11. Air entering the rotor at absolute stagnation pressure P_{in} may be envisioned as undergoing a reduction in stagnation pressure due to the change to relative coordinates, an increase in stagnation pressure due to the flat plate compressor effect, and a

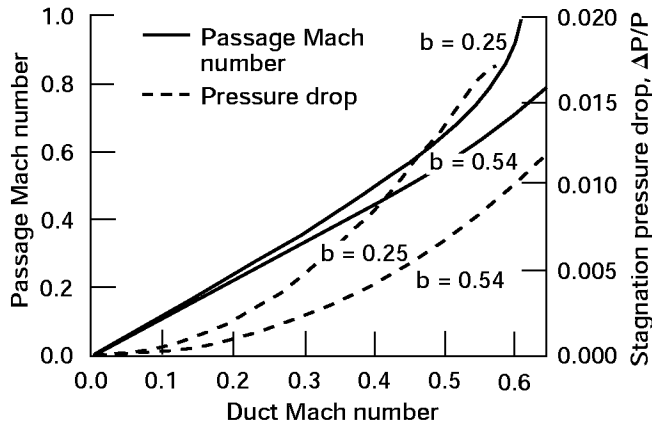


Figure 9.—Stagnation pressure drop and passage Mach number versus the duct axial Mach number for entry into the rotor passages for the two passage widths used in the experiment.

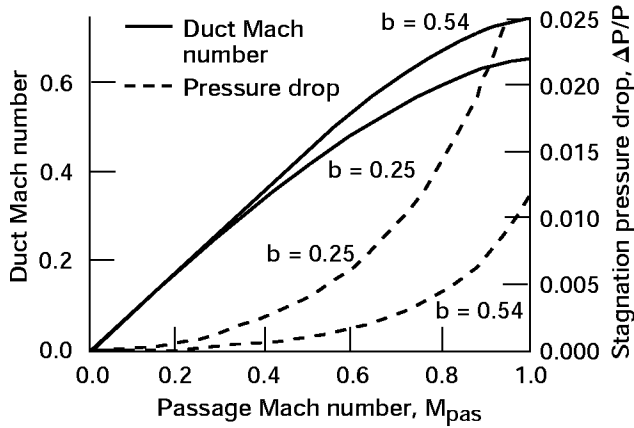


Figure 10.—Stagnation pressure drop and duct axial Mach number versus passage Mach number for exit from the rotor passages for the two passage widths used in the experiment.

decrease in stagnation pressure due to incidence losses, coupled with a small entrance loss (omitted in fig. 11). Of course, these effects do not take place sequentially, they are all part of the same event. The resulting relative stagnation pressure is Pr_{in} .

Within the wave rotor there are losses due to leakage, finite opening time, and boundary layers, together with losses due to wave effects, including the loss as the nonuniform flow in the low-pressure port mixes to a uniform distribution. At the exit ports, the relative stagnation pressures will be Pr_{hi} and Pr_{lo} . On leaving the wave rotor there will be losses in each port due to exiting the passages (also omitted in fig. 11), and stagnation pressure increases on changing to the absolute frame, leading to the measured P_{hi} and P_{lo} .

The measured P_{in} can be corrected to Pr_{in} if f is known by accounting for the flat plate compressor effect, including incidence loss, and subtracting the entrance loss. Similarly, the exit

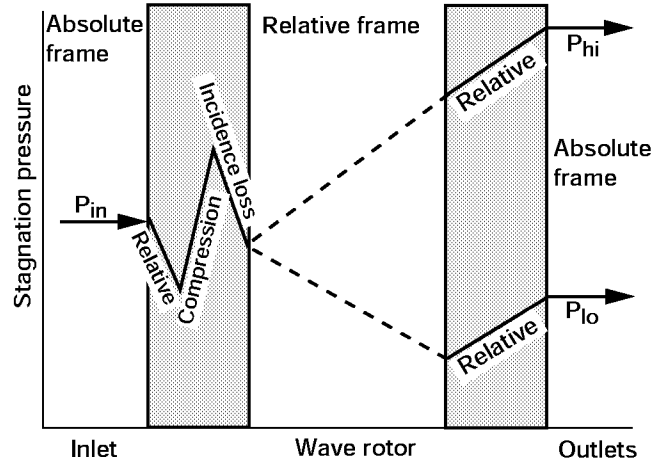


Figure 11.—Diagram illustrating the stagnation pressure changes as air flows through the wave rotor. The entry and exit losses have been omitted.

pressures can be referred to the relative frame, and the exit losses added to provide Pr_{hi} and Pr_{lo} . The corrected relative efficiency will then be found by using the values of Pr_{in} , Pr_{hi} , and Pr_{lo} in equation (1).

Experimental Design

Statistical Experiment

In order to obtain experimental values of the losses due to opening time, friction, and port and wall leakage, the parameters τ , F , G_p , and G_w must be varied. An efficient way to formulate an experiment to obtain empirical fits to data when there are three or more variable parameters is the Box-Behnken scheme (Box and Behnken, 1960). This scheme is illustrated for three variables in figure 12. Imagine a box, each side of which extends from the minimum value of the corresponding parameter to the maximum value of the parameter. Experimental readings are taken at the points indicated in the middle of each side, together with three replicate points at the center of the box. It is then possible to fit the results with a second-degree polynomial. For example, if the measured dependent variable is the efficiency η , and the independent variables are τ , F , and G , then the fit will be of the form

$$\eta = b_0 + b_1\tau + b_2F + b_3G + b_{11}\tau^2 + b_{22}F^2 + b_{33}G^2 + b_{12}\tau F + b_{13}\tau G + b_{23}FG \quad (35)$$

where the constants b_0 , b_i , and b_{ii} are determined from the experimental measurements. The replication of the center point provides an estimate of the experimental error. The

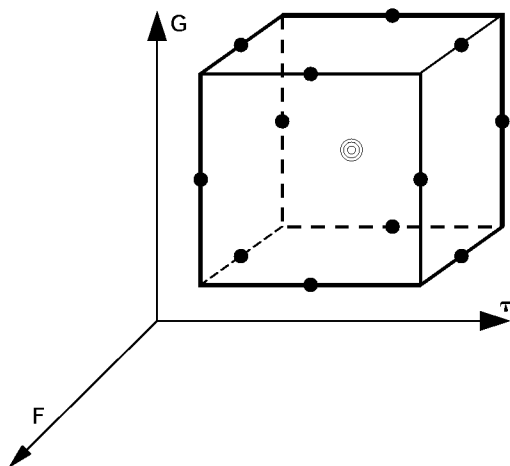


Figure 12.—Illustration of the Box-Behnken design of an experiment with three variables. Runs are made at values of the variables corresponding to the solid circles shown. In addition, the center point, indicated by three concentric circles, is run three times.

scheme for four variables is equivalent, but harder to illustrate since drawing a four-dimensional box is rather difficult.

The present wave rotor experiment was formulated as a four variable design, with τ , F , G_p , and G_w as the independent variables. The dependent variable, or response, was taken to be the efficiency. The set of runs that must be made in order to evaluate the constants was determined using commercial software (Seshadri and Deming, 1990), and is listed in table II. RS/Explore software was used to determine the constants from the experimental data.

In designing the experiment, the actual rotor dimensions had to be determined. A review of the literature showed that the geometry had differed significantly for rotors built in the past: sometimes with no indication of the value of the end wall to rotor gaps. The details of several past rotors are given in table III. The nondimensional opening time τ has varied over a range of 0.1 to 0.35. The major component of the friction parameter, namely the ratio L/D_h , has varied between 3.7 and 84. Finally, the leakage parameter G (previous workers have not differentiated between G_p and G_w) has varied from 0.005 to 0.017. The objective in designing this experiment was to cover as much of this range as possible.

In order to cover as much of the parameter range as possible, the actual experiment consisted of two different rotors, both 12 in. in diameter, but one 18-in. long and the other 9-in. long.

TABLE II.—SET OF RUNS FOR THE STATISTICAL EXPERIMENT

Run number *	Rotor length, in.	Passage width, in.	n	RPM	Port gap, in.	Wall gap, in.	P_{in}
1	18	0.25	1.5	3700	0.010	0.010	30
2	18	0.25	3.0	1850	0.005	0.010	30
3	18	0.25	3.0	1850	0.015	0.010	30
4	18	0.25	3.0	1850	0.010	0.005	30
5	18	0.25	3.0	1850	0.010	0.015	30
6	9	0.25	1.5	7400	0.010	0.010	38
7	9	0.25	1.5	7400	0.010	0.005	30
8	9	0.25	1.5	7400	0.010	0.015	30
9	9	0.25	1.5	7400	0.005	0.010	30
10	9	0.25	1.5	7400	0.015	0.010	30
11	18	0.54	1.5	3700	0.010	0.010	30
12	18	0.54	1.5	3700	0.005	0.005	30
13	18	0.54	1.5	3700	0.015	0.005	30
14	18	0.54	1.5	3700	0.015	0.015	30
15	18	0.54	1.5	3700	0.005	0.015	30
16	18	0.54	1.5	3700	0.010	0.010	30
17	18	0.54	3.0	1850	0.010	0.005	30
18	18	0.54	3.0	1850	0.010	0.015	30
19	18	0.54	3.0	1850	0.005	0.010	30
20	18	0.54	3.0	1850	0.015	0.010	30
21	18	0.54	3.0	1850	0.010	0.010	15
22	18	0.54	3.0	1850	0.010	0.010	53
23	18	0.54	1.5	3700	0.010	0.010	30
24	9	0.54	1.5	7400	0.005	0.010	30
25	9	0.54	1.5	7400	0.015	0.010	30
26	9	0.54	1.5	7400	0.010	0.005	30
27	9	0.54	1.5	7400	0.010	0.015	30

*Runs 11, 16 and 23 are replicates.

TABLE III.—COMPARISON OF DIFFERENT WAVE ROTORS

Machine type	Thayer Pressure exchanger	Weatherston Pressure exchanger	Pearson Wave turbine	Hoerler Pressure exchanger	Kentfield Flow divider	This work Flow divider
Length (L), in.	15.8	66	3.5	4.25	11	9.18
Diameter (D), in.	14.4	60	9	3.23	8	12
Passage width (B), in.	0.4	0.55	0.7	0.19	0.66	0.25, 0.54
Passage height (H), in.	1.5	1.43	1.5	1.1	2.2	0.4
Hydraulic diam, (D_h), in.	0.63	0.79	0.95	0.32	1.05	0.31, 0.46
RPM	1960	2700	18000	11200	5500	1850 to 7400
Cycles/revolution, n	2.5	1	1	2	3	1.5, 3
Leakage gap (δ), in.	0.004–0.013	—	—	0.004	0.007	0.005, 0.01, 0.015
Ratio (L/D_h)	25	84	3.7	13	10.5	20–58
Ratio ($2\delta/H$)	0.005–0.017	—	—	0.007	0.006	0.025 to 0.075
Opening time (τ)	0.2	0.1	0.3	0.33	0.35	0.08 to 0.35

TABLE IV.—PORT TIMING AND DUCT ANGLES

Run	Inlet port			High-pressure port			Low-pressure port		
Angle type									
	Opening	Closing	Duct	Opening	Closing	Duct	Opening	Closing	Duct
1	108°	172°	22°	129°	194°	47°	0°	70°	13°
2-5	55°	86°	11°	66°	96.5°	28°	0°	35°	6.5°
6-10	108°	172°	36°	129°	194°	65°	0°	70°	27°
11-16,23	108°	169°	22°	129°	190°	47°	0°	70°	13°
17-22	55°	84°	11°	67°	93°	28°	0°	35°	6.5°
24-27	108°	172°	36°	129°	190°	65°	0°	70°	27°

Both were built with 0.25-in.-wide passages and were 0.4-in. high with 120 passages per rotor. After a series of runs at 0.25-in. passage width, every other wall was removed, and another series of runs was made at approximately twice the passage width. Ducts were designed for operation at $n = 1.5$ for both the 9- and 18-in.-long rotors. Adding a different set of ducts for operation at $n = 3$ with the 18-in. rotor provided a combination giving three values of τ , and three values of L/D_h , covering the range 20 to 58, and hence, three values of F . For runs 6, 21, and 22, the geometry changes did not give the value of F called for by the statistical formulation. Instead, inlet pressure variation was used to get closer to the desired value from the closest available value. The value of $n = 1.5$, rather than $n = 1$, was used to provide a long region between closing of the high-pressure port and opening of the low-pressure port to allow any remaining waves to die out, and give the uniformity prior to opening the low-pressure port that was assumed in calculating the cycle. In fact, only one actual cycle was used; what is meant by $n = 1.5$ and $n = 3$ is the number of cycles there could be per revolution at the timing used for the one cycle. In order to vary the port leakage gaps, the ports were built as inserts supported on a flange. Placing shims under the flange permitted variation of the rotor to port gaps. The rotor to wall gap was varied by providing moveable end walls at each end, consisting of disks, which could move axially. Springs at three locations pushed the disks away from the rotor, and three screws forced the disks toward the rotor. Adjustment of the screws gave the desired gap spacing. The minimum spacing that could be used safely was 0.005 in., larger than had been hoped for. This gave a value of

$G = 0.025$, which was greater than the values used by other workers, due to the small passage height of the present experiment.

The port geometries for all the runs are given in table IV. What is listed is the circumferential angle at which each port opens and closes, measured in the direction of rotation from the opening of the low-pressure port. Also given are the duct angles, which are the angles made by the centerlines of the ducts to the rotor axis. The port height is the same as the passage height.

Air was supplied to the rotor from an in-house system at 55 psia. To prevent condensation in the low-pressure leg, the air was heated before going to the rotor. The heater was controlled to give an inlet temperature of 580 °R. Control of the wave rotor flows was by a butterfly valve in each leg. The inlet valve was adjusted to throttle the supply pressure down to the desired inlet stagnation pressure, usually 30 psia. The expansion ratio was set by the low-pressure valve, based on a low-pressure port static pressure reading, and a pressure tap in the inlet end wall giving the passage pressure just before opening to the low-pressure port. The high-pressure valve controlled the mass ratio, based on the input and high-pressure orifice mass flow readings. The rotor was turned by a variable speed electric motor with a constant speed control. An independent measurement of the rotor speed was also made. Toward the end of the tests, a power meter was added to measure the electrical power provided to the motor.

A photograph of the apparatus, with the 18-in. rotor in place, is shown in figure 13. Figure 14 shows a view of the 18-in. rotor on the balancing machine.

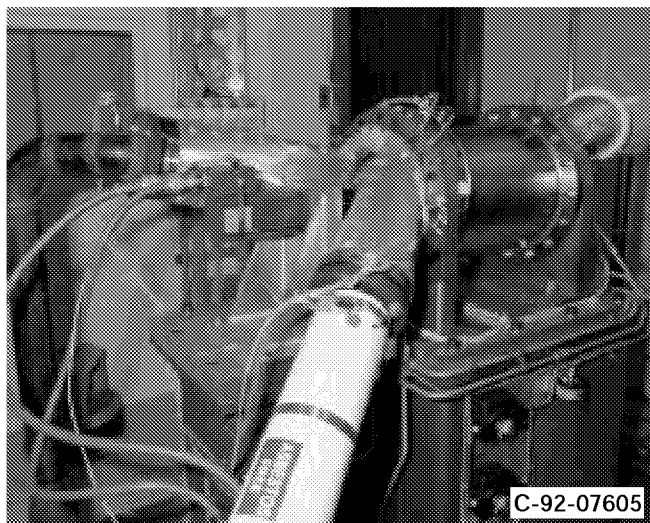


Figure 13.—The three-port flow divider apparatus.

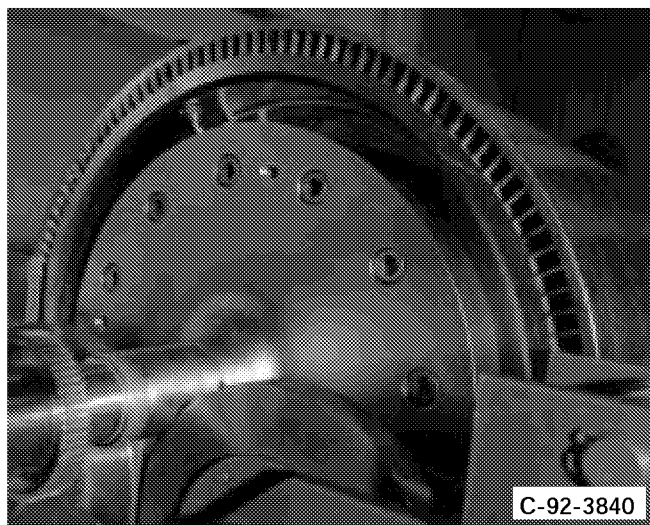


Figure 14.—The 18-in. rotor with the 0.25-in.-wide passages on the balancing machine. A dynamic pressure transducer can be seen inside the rotor at the upper left.

Additional Tests

In addition to the statistical experiment, three other tests were performed. The first was to see whether brush seals could prevent leakage, the second was to see whether inlet pressure variation would have any significance, and the third was to examine the effect of changing the radius of the inlet port leading edge rounding.

For the leakage test, brush seals were designed to fit around the inner and outer diameters of the rotor passages. The seals were fastened to the end walls, with the brushes rubbing on the appropriate diameter. A drawing of the downstream end wall showing the location of the seals is given in figure 15. Identical

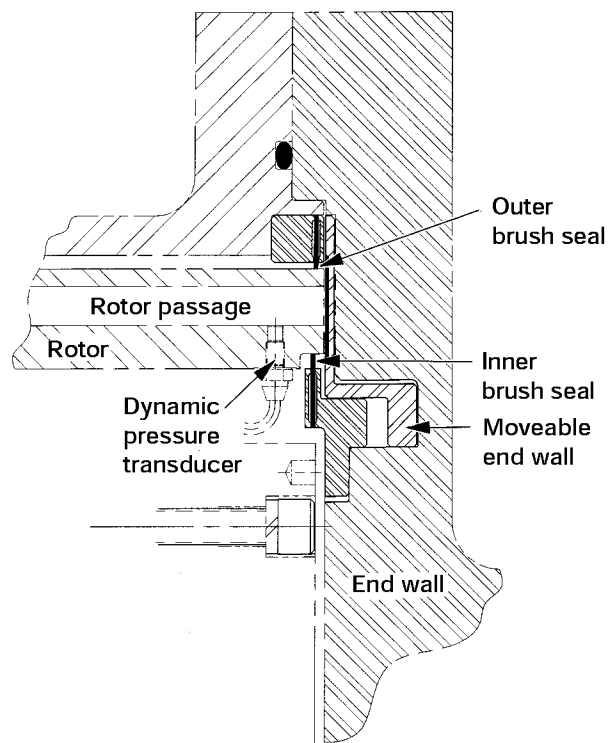


Figure 15.—A cross-sectional view of the rotor and end wall showing the location of the inner and outer brush seals.

brush seals were installed at the other end. Photographs of the inner and outer seals are given in figures 16 and 17 respectively, with a closeup of the brushes in figure 18. The seals consisted of packed bristles, 0.0028-in. diameter, made of Haynes 25 AMS 5796. The bristle density was 2250 to 2650 wires per inch of bare circumference. The bristles were at an angle of about 45° to the radius, inclined with the flow, i.e., the rotor moves counterclockwise in figure 18. The seals were manufactured by Cross Manufacturing Company.* The purpose of the seals was to prevent leakage from the passages to the surrounding cavity and vice-versa. The seals cannot prevent passage to passage leakage. The seals were installed on the 9-in. rotor, and tests were made in which the performance, (i.e., P_{hi} , P_{lo}) was measured for values of ϵ between 0.33 and 0.8, for equal wall and port gaps of 0.015, 0.010, and 0.005 in., at $\beta = 0.37$, so that the results could be compared with the corresponding runs without brush seals made during the statistical experiment.

Although some pressure variation had been done during the statistical experiment, it was not extensive. It was hoped that a more complete variation of pressure only might indicate whether the flow was laminar or turbulent. Consequently, a set of runs was made with the 9-in. rotor, at equal wall and port settings of 0.010 in., $\beta = 0.37$, covering as much as possible of the range of ϵ between 0.33 and 0.8, at inlet pressures of 10, 14, 30, and 38 psi.

*Cross Manufacturing Co. (1938) LTD., Bath Rd., Devizes, Wilts, SN10 1QD, England.

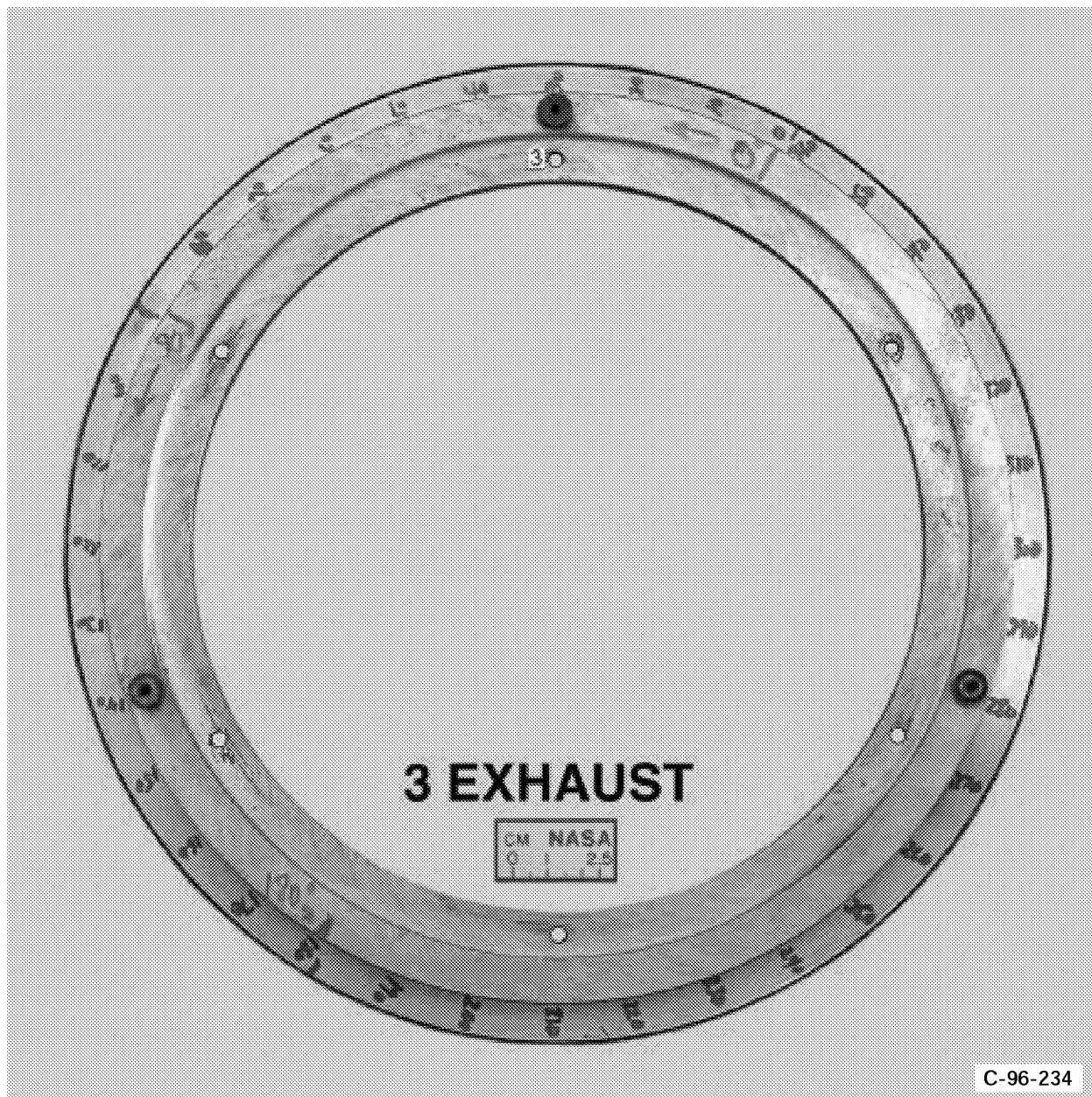


Figure 16.—The inner diameter brush seal.

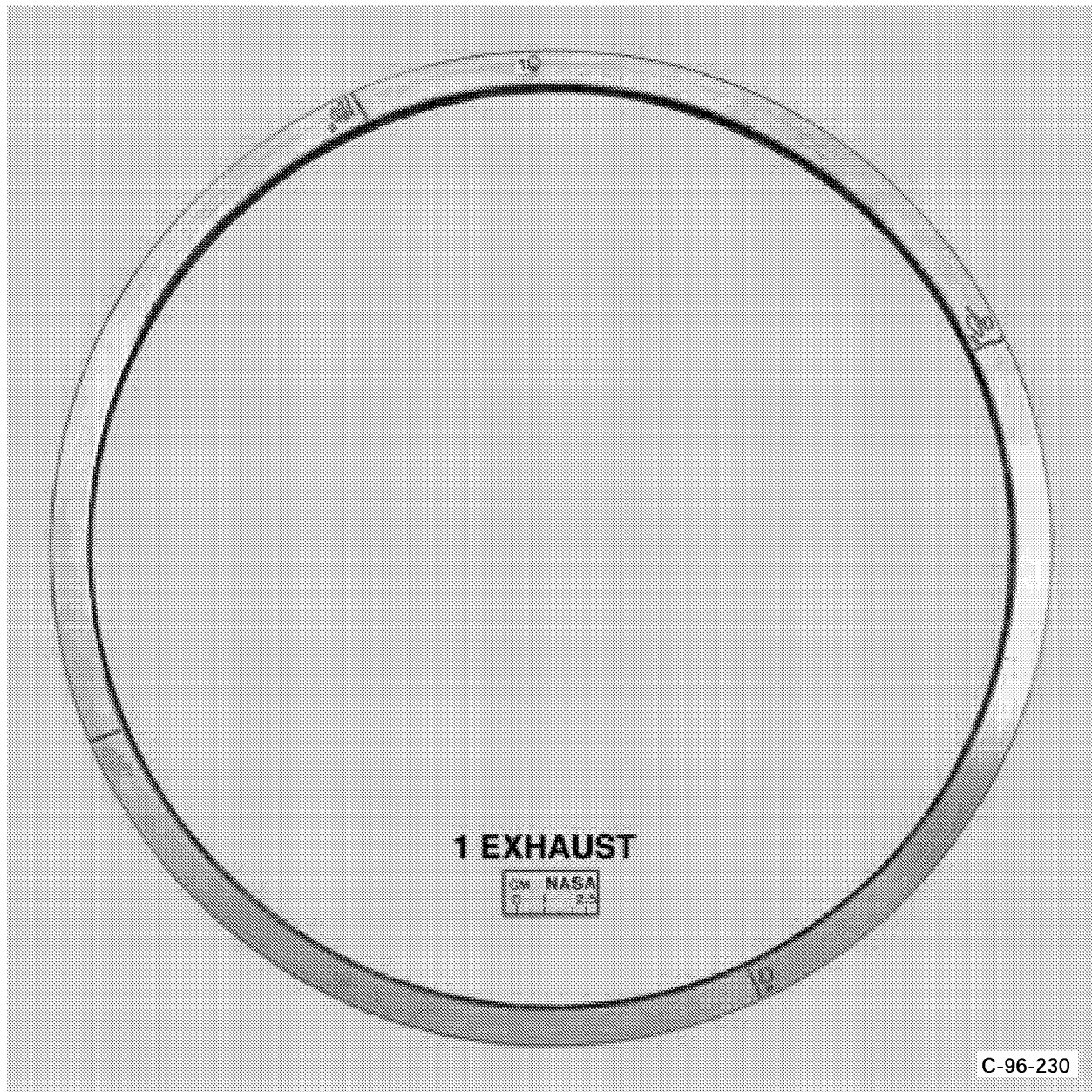


Figure 17.—The outer diameter brush seal.

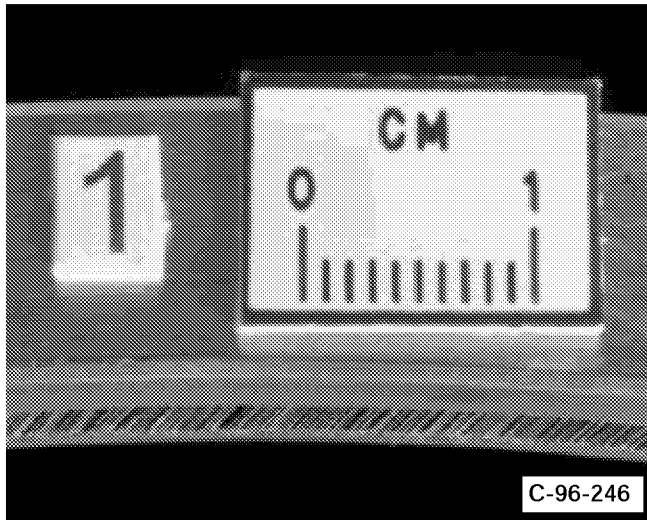


Figure 18.—Closeup view of the outer brush seal. Rotor rotation in this view is counterclockwise.

In all the tests described so far, the radius of the inlet port leading edge rounding was held constant at 1.62 in., as shown in figure 7. Since this rounding could affect performance, the effect of changing the value of the inlet port leading edge radius was investigated by running tests at different values of this radius. In order to accommodate the changing duct angles in the statistical experiment, the leading edge of the inlet port had been made as an insert. Thus, it was comparatively easy to make

new inserts with different radii. Inserts with radii of 0.44, 0.22, 0.11, and 0 in. were made. The geometry of these inserts is shown in figure 19. Because the opening of the inlet port is delayed as the radius gets smaller, slivers were also inserted into the high-pressure port to delay its opening. The closing of the ports could not be changed, which introduced an undesirable change into the timing. Tests were run at equal wall and port gaps of 0.005 in., varying ϵ between 0.33 and 0.8, at a value of $\beta = 0.37$, for each of the radii. The 9-in. rotor with 0.54-in.-wide passages was used for these tests with an inlet duct angle of 36° .

Experimental Measurements

The efficiency of the flow divider (eq. (1)) is determined by the ratios of P_{hi}/P_{in} and P_{lo}/P_{in} at a particular value of β .

Higher values of both ratios correspond to higher efficiency. The necessary measurements are the mass flows in each port and the stagnation pressures of the inlet, high-pressure, and low-pressure flows. The instrumentation is indicated in figure 20. The mass flows were measured with standard orifice meters, and the ports are obviously sections of an annulus. A transition piece in front of the inlet port took the flow in the inlet pipe and converted it to the port shape accelerating the flow in the process as well as bringing it onto the rotor at the correct angle. Immediately upstream of the transition piece but downstream from the orifice was a diagnostic spool, with three wall static taps, five pitot tubes, and a thermocouple. The inlet

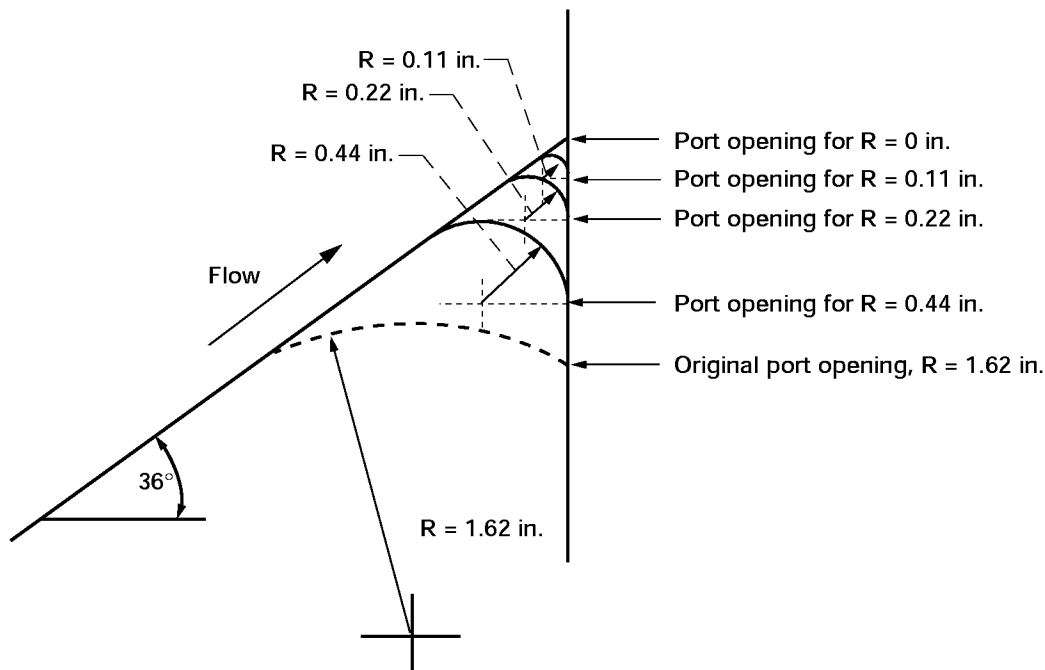


Figure 19.—The geometry of the inlet port leading edge for different values of the radius of the rounding.

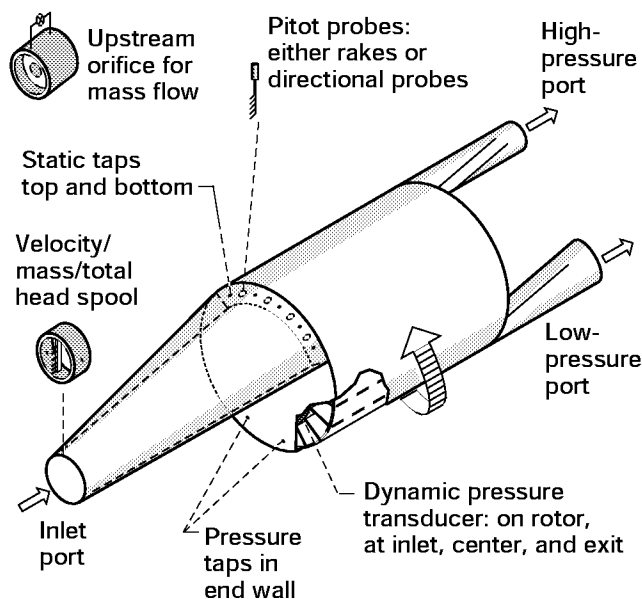


Figure 20.—The apparatus with the diagnostic equipment added.

stagnation pressure and temperature were determined by measurements at this spool. Similarly, the output ports had transition pieces to take the flow from the port shape back to round, and which also acted as diffusers. The downstream area of these diffusers was fixed by the exhaust pipe diameter. With the diffuser area ratio determined, the length was chosen to give maximum diffuser efficiency using the diffuser performance curves of Mattingly, et al. (1987). A diagnostic spool was placed immediately at the exit of each diffuser with the intention of using the measurements to evaluate exit stagnation pressures. However, the velocity distribution was found to be nonuniform, and it was not clear whether the resulting stagnation pressure would be reliable. Instead, measurements made at the ports were used to calculate a stagnation pressure.

There were five static pressure taps on the top and bottom of each port and four pitot tube installations. The pitot installations carried either a rake of five pitot tubes to determine radial velocity distribution, or a tube-type combination probe (Glawe and Krause, 1974) to determine centerline velocity and direction. In addition, for some runs three pitot probes were located on the port centerline at the leading and trailing edges of the inlet port, spaced 0.12, 0.24, and 0.36 in. from the wall, to provide wall velocities in these regions. In the high-pressure port, velocities are low and relatively uniform and an average of the individual port stagnation pressure measurements was taken as the port stagnation pressure. In the low-pressure port, the velocity distribution is very nonuniform both radially and circumferentially. The measurements were used to create a circumferential velocity distribution, and also, by using a rake probe, to create a radial velocity distribution. These distributions were used to create mass, momentum, and energy integrals for a mixing calculation (Foa, 1960), from which the

stagnation pressure for a uniform downstream velocity was evaluated and used as the low-pressure port stagnation pressure. The pressure measurements were steady state. For some runs, a dynamic pressure transducer was installed 4 in. downstream of the low-pressure port. The signal from this transducer was a sine wave at the passage passing frequency with a peak to peak value of 0.5 percent of the steady-state pressure. Thus the pressures were essentially steady state.

All steady-state pressure measurements were recorded through an electronically scanned pressure (ESP) measurement system. The pressure measuring system automatically self-calibrates every 20 min to maintain a 0.2-percent accuracy. The ESP system communicates through an Institute of Electrical and Electronics Engineers 488 interface to a state-of-the-art, real-time data acquisition system designed at NASA Lewis (Fronek, et al., 1987). The data system was designed for small to medium sized aeronautics facilities, most of which are currently testing rotating machinery. The system acquires data, converts the data to engineering units, computes test dependent performance calculations, and displays the information in alphanumeric or graphical form. The cycle time is 1 sec.

Another important measurement was the dynamic onboard rotor pressure. Six dynamic pressure transducers (Endevco Model 8530 with 100-kHz response) were fitted into the rotor. Two were near the entrance to the passages, two in the center, and two near the exit (see fig. 19). One set (entrance, center, exit) was in one passage, the other set in a passage diametrically opposed to the first set. The transducers were mounted flush with the lower wall of the passage. The signals from the transducers were taken off the rotor through a slip ring, displayed on a Tektronix oscilloscope, and recorded on tape. These measurements were used for comparisons of the actual pressure history with that calculated for the postulated cycle.

Results

Dynamic Pressure Traces

An oscillogram of the inlet and exit onboard pressure transducer signals obtained in an early run is shown in figure 21(a). The inlet signal shows that the pressure is reasonably uniform before the arrival of the expansion wave caused by the opening of the low-pressure port. When that wave arrives, the pressure drops falling to a value below that of the low-pressure port. Opening of the inlet port causes the main shock to be propagated into the passage. Arrival of the reflected shock is seen briefly before the inlet port closes, creating the second expansion which brings the flow to rest.

On the exit side, the pressure is constant prior to the opening of the low-pressure port, then drops to the port value. Later, the high-pressure port opens at the same time that the main shock is reflected, raising the pressure above the inlet pressure. The pressure falls again when the port closes simultaneously with

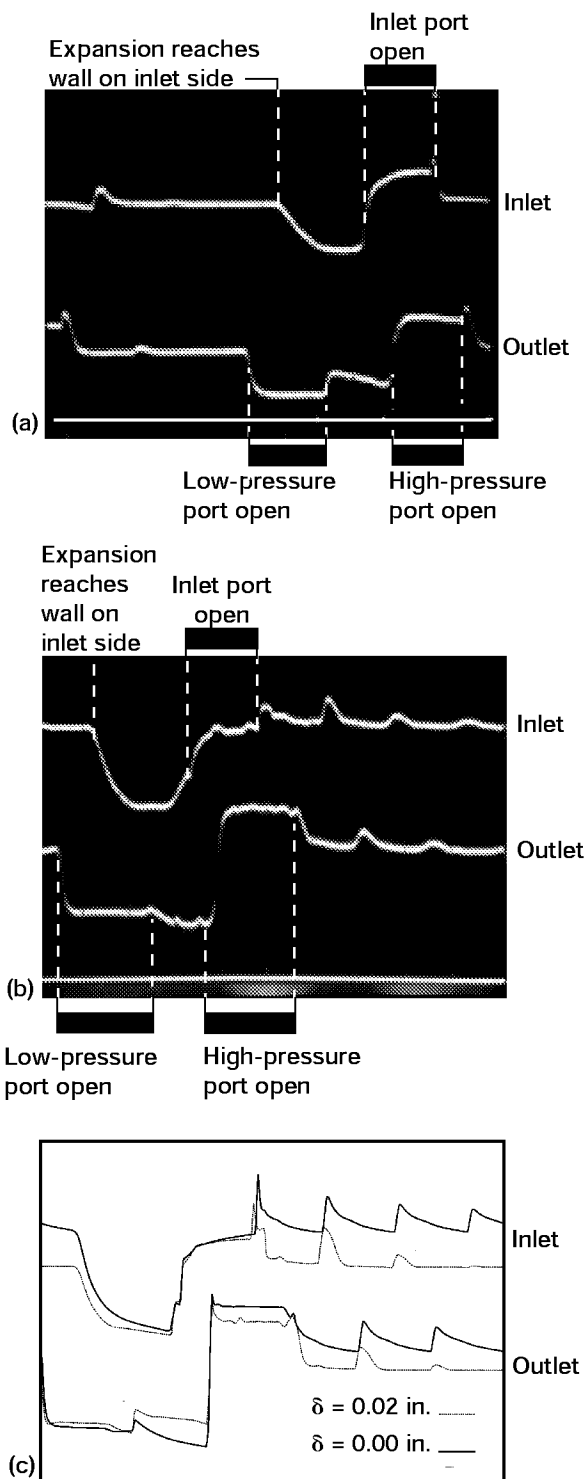


Figure 21.—Oscillograms of the signals from dynamic pressure transducers mounted onboard the rotor at the inlet and outlet ends of the rotor showing pressure (ordinate) versus time (abscissa) for (a) an early run with rotor to end-wall spacing of 0.020 in. (b) a later run with a rotor to each-wall spacing of 0.005 in., and (c) calculated pressure time plots.

the arrival of the second expansion. This is apparently in agreement with the postulated cycle as shown in figures 3 and 4. Also shown in figure 21(c) are two sets of calculated pressure traces, generated with the 1-D CFD code of Paxson (1995), one for no leakage, and the other for a leakage gap of 0.020 in. With no leakage, following the closing of the low-pressure port, the calculated pressure on the outlet side, after a brief rise, falls, dropping to a value below that in the low-pressure port, and only rising again when the main shock arrives. This differs from the oscillogram of the early run, in which the pressure is seen to rise significantly, simultaneously with the closing of the low-pressure port, and never falls below the level in the low-pressure port. This pressure rise is caused by a shock wave generated by the low-pressure port closing. The reason for this shock is seen in figure 22 which gives the measured velocity as a function of position in the low-pressure port. The calculation of the cycle by characteristics and CFD put the closing of the low-pressure port at the position where the reflected expansion wave had reduced the velocity to zero. The measured velocity is clearly not zero at port closing. Closing the passage when an outward velocity remains generates a hammer shock in order to bring the gas to rest.

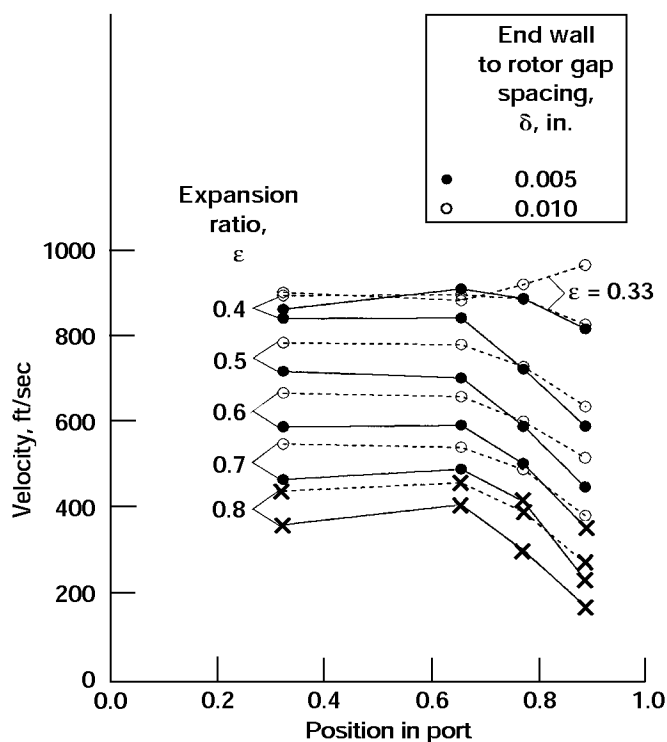


Figure 22.—Flow velocities measured in the low-pressure (outlet) port. The data were taken with the 9-in. rotor with 0.54-in.-wide passages. The measurements indicated by a cross are erroneous readings. There was a large difference between the flow and the probe angles for the erroneous points leading to a low indicated velocity.

Calculations using the CFD code of Paxson (1995) were made to try to explain why the gas still had a significant outward velocity at port closing in the experiment but not in the theory. The CFD calculation includes finite opening, friction, and, originally, only port gap leakage losses. Even when these losses were set at higher values than expected, it was not possible to create a significant hammer shock at the port closing. However, when end-wall leakage was included, a strong shock did appear, as shown in the calculated pressure trace for a gap of 0.020 in. This is explained as follows: when the expansion wave reaches the wall at the inlet side, the pressure in the passages drops rapidly and falls below the value in the rotor casing, thus ingesting air into the passages from the casing through the rotor-wall gap. This sets up an outward velocity in the passages, which is not cancelled by the reflected expansion wave. Consequently, there is still velocity in the passages when the port closes giving rise to the hammer shock. The magnitude of this leakage is a function of the rotor-wall gap, and this gap plays a larger role than the gap at the ports. To confirm this conclusion, an oscillogram from a later run with much smaller wall gap is shown in figure 21(b). As seen from figure 22, reducing the wall gap reduces the velocity at port closing as would be expected if this residual velocity were a consequence of leakage. Although the oscillogram of the later run still shows some evidence of a hammer shock, it is much weaker, as would be expected if the velocity at low-pressure port closing is smaller. In fact, the pressure trace is quite close to the calculated pressure trace for no leakage. Bearing in mind that the pressure transducers have a finite response time, so that sharp changes are smoothed out, the agreement between the measured and calculated pressures is quite remarkable.

Statistical Experiment

For the statistical experiment, runs were made at a nominally constant value of $\beta = 0.37$ (the design value) mostly at an input stagnation pressure of 30 psia, varying ϵ from 0.33 to 0.8, unless the full range was not accessible. Because it was not possible to achieve $\beta = 0.37$ exactly on every run, runs were also made at a nominal $\beta = 0.36$, and $\beta = 0.38$. From these extra runs, a local value of the derivatives of P_{hi}/P_{in} and P_{lo}/P_{in} with respect to β could be calculated, and used to correct the measured values to values corresponding to $\beta = 0.37$ exactly. The data are given in the appendix.

The results were plotted as P_{hi}/P_{in} versus P_{lo}/P_{in} . A sample of the results showing performance changes for the different rotors, with both port and wall gaps set equal to 0.010 in., is given in figure 23(a). All these runs were made at an inlet stagnation pressure of 30 psia. The runs made with the 18-in. rotor at $n = 3$ have a larger opening time than the runs with $n = 1.5$ but the same value of friction factor. Thus it is seen that increasing the opening time reduces performance. Runs with the wider passages are superior in performance to runs made

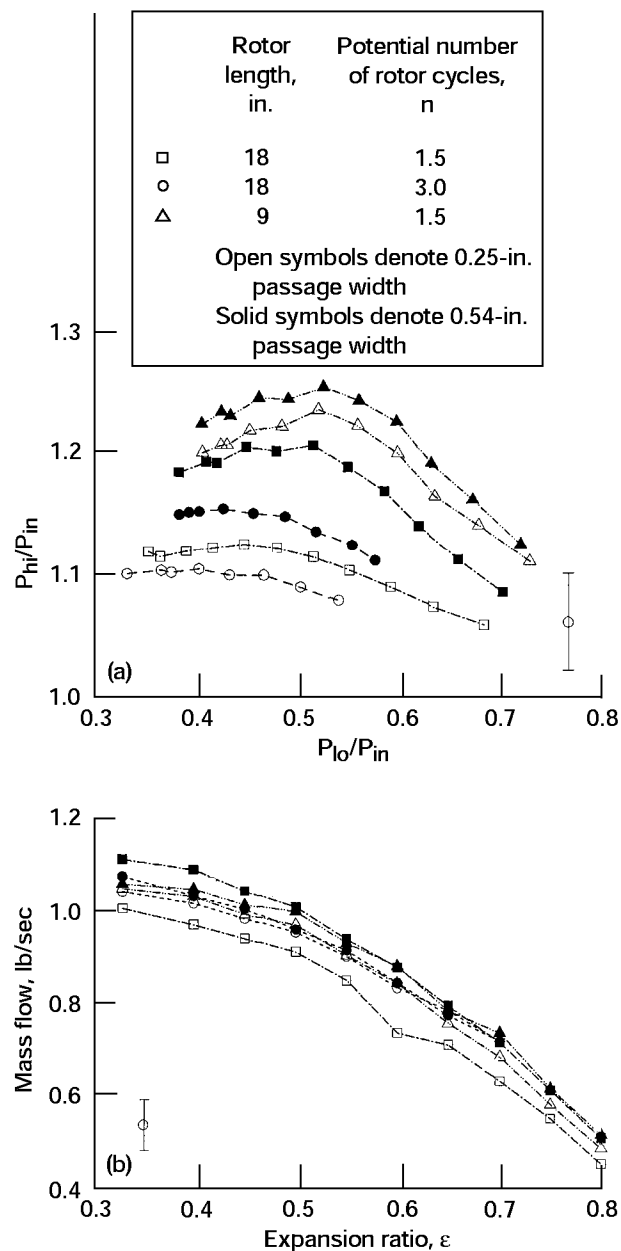


Figure 23.—(a) A summary of the experimental results showing the variation in flow-divider performance with changes in opening time and passage length and width and (b) the corresponding changes in mass flow. All runs had a gap spacing of 0.010 in.

with the narrow passages. The runs with the wider passages have a larger opening time, but lower friction factor than the runs with the narrow passages. For these runs then, reduction in friction is more beneficial than the increase in opening time is deleterious. This is more evident for the runs with the 18-in. rotor than it is for the runs with the 9-in. rotor, indicating that friction is becoming less important for the shorter rotor. The

estimated experimental error, expressed as 95-percent confidence limits, is indicated by the error bars in figure 23(a). At 95-percent confidence, the 9-in. rotor has significantly greater performance than the 18-in. rotor except for the 18-in. rotor with 0.54-in. passages and $n = 1.5$. The 9-in. rotor with 0.54-in.-wide passages does have significantly greater performance than the 18-in. rotor with 0.54-in. passages and $n = 1.5$ at 82 percent confidence. With the 9-in. rotor the maximum value of P_{hi}/P_{in} occurs at an expansion ratio of 0.55, whereas the maximum efficiency is at an expansion ratio of 0.65. The performance curves have the same shape as the curves of figure 2(b), but are lower than the (interpolated) curve for $\beta = 0.37$, indicating that there are indeed additional losses.

Results obtained with the 18-in. rotor at three different gap spacings are shown in figure 24(a). The three runs at a gap spacing of 0.010 in. are the replicated runs at the center point from which the total error can be calculated and is shown by the error bar in figure 24(a), indicating 95-percent confidence limits. The change in performance caused by a gap change of 0.005 in. is greater than the experimental error so the observed effect is real. During any run, the point at an expansion ratio of 0.6 was repeated five times. From these measurements, the standard deviation of P_{hi}/P_{in} was of the order of 0.003 (the error in P_{lo}/P_{in} was much less). These measurements were at a fixed gap setting, and so the error corresponds to the error of reproducibility of the measurements for a fixed gap setting. The three replicated runs, though nominally at the same gap setting, exhibit a larger error with a standard deviation of approximately 0.012. The only difference between the replicates was the actual value of the gap setting, since it was not possible to reset a gap exactly. From this, it can be concluded that the largest source of error was caused by the inability to provide an accurate gap setting. There is a significant increase in performance as the gap spacing is reduced.

Mass Flow

Although the changes in passage length and width did result in quite large changes in performance, as shown in figure 23(a), the resulting changes in mass flow, shown in figure 23(b), were not so large. Nor are the trends so clear-cut. It might be expected that the mass flow would increase as the losses decreased, as was the case for the performance. However, the greatest mass flow was observed for the 18-in. rotor with 0.54-in. passages at $n = 1.5$ and the smallest mass flow was also for the 18-in. rotor at $n = 1.5$ but with the 0.25-in. passages. Most of the changes seen were not statistically significant at the 95-percent confidence level, but the changes described above for the 18-in. rotor were, so this result is puzzling.

The mass flow also changed with end wall to rotor gap spacing (as shown in figure 24(b)). For values of expansion ratio lower than 0.5, the trends are as would be expected, i.e., as the gap was reduced, the mass flow increased. However, at

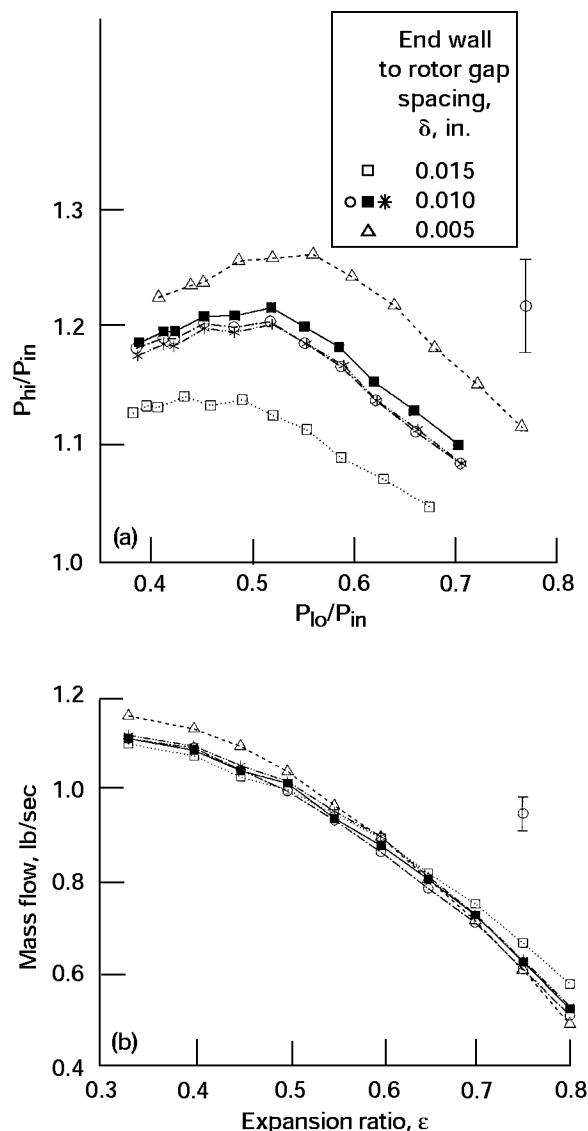


Figure 24.— A summary of the experimental results, obtained while varying the leakage gap (i.e., rotor to end-wall spacing). The results for a gap of 0.010 in. represent the center point of the statistical experiment which was run three times. (a) The wave rotor performance and (b) corresponding mass flows. These data were taken with the 18-in. rotor, with a 0.54-in. passage width.

an expansion ratio of 0.8, the exact opposite is seen. Again, most of the results were not statistically significantly different from one another, but the increased mass flow for the 0.005-in. gap for expansion ratios of 0.45 and below, and the increased mass flow for the 0.015-in. gap at an expansion ratio of 0.8, were significantly different at about 85 percent confidence.

The mass flow clearly decreases with increasing expansion ratio.

Flow Velocities

Values of the velocities measured at the average diameter at the four total pressure probe locations in the inlet port are shown in figure 25. The probes are positioned 0.85 in. upstream of the rotor face. These velocities were measured using the 9-in. rotor with the 0.54-in.-wide passages both for small ($\delta_p = \delta_w = 0.005$ in.), and large ($\delta_w = \delta_p = 0.0015$ in.) leakage gaps. Leakage decreases the velocity for values of $\epsilon = 0.5$ or lower but increases the velocity for ϵ closer to unity. This is consistent with the effect of leakage on mass flow. The velocity at the leading edge of the port is quite high. This is a consequence of the flow's being accelerated by the low pressure in the passage entering the inlet port around the leading edge rounding of the inlet port. It has been reproduced in two-dimensional CFD computations (Welch, 1996).

Velocities measured at the average diameter at the four total pressure probe locations in the low-pressure port are shown in figure 22. Note that there is a problem with the velocity measurements of figure 22 at $\epsilon = 0.6, 0.7$, and 0.8 . Velocities less than the rotor speed of 388 ft/sec were deduced from the data. These values are not realistic. Total pressure probes are accurate up to about 15° angle of attack but indicate a reduced pressure beyond that angle. For $\epsilon = 0.6$, the fourth probe is at 20° to the flow, for $\epsilon = 0.7$, the third probe is at 24° to the flow and the fourth probe at 34° , and for $\epsilon = 0.8$, the first probe is at 30° to the flow and the third probe is at 44° , and the fourth probe is beyond 45° . All of these probes will be giving low total pressure readings and hence, low velocities. By comparing

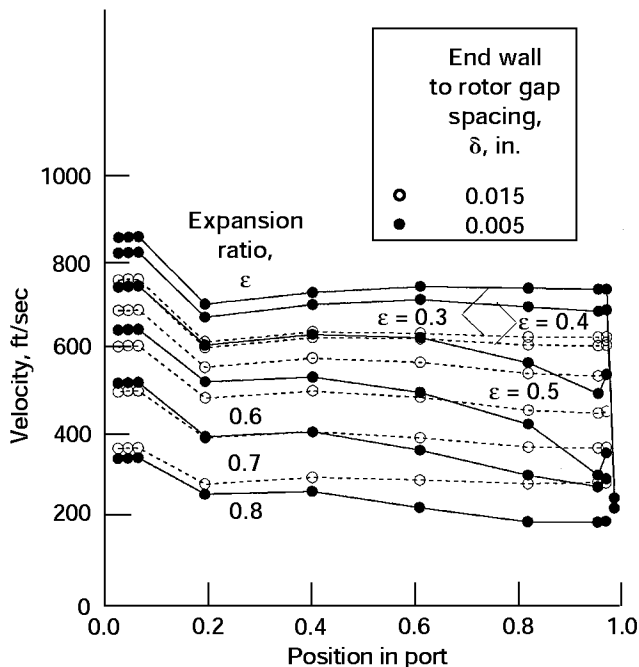


Figure 25.—Flow velocities in the inlet port for the 9-in. rotor. The data were taken with the 9-in. rotor with 0.54-in.-wide passages.

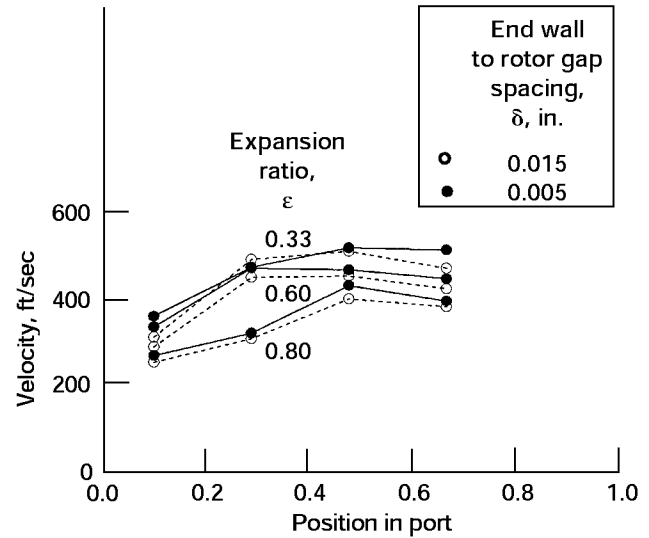


Figure 26.—Observed distributions of centerline velocity in the high-pressure outlet port as a function of position in the port. These results were measured using the 9-in.-rotor with 0.54-in.-wide passages.

figure 22 with figure 25, it can be seen that for all the cases shown, the velocities in the low-pressure port were greater than those in the inlet port. This is contrary to the predictions of the isentropic calculation but in agreement with calculations for the ideal cycle and the real cycle (that is, including losses). Leakage causes the velocity in the low-pressure port to increase, particularly at the trailing edge of the port.

The velocity distribution in the high-pressure port is shown in figure 26. The high-pressure port velocities are lower than the velocities in the other ports, and are much less affected by expansion ratio and leakage.

Radial Velocity Distribution

Measurements of the distribution of velocity with radius, that is, height in the passage, are shown in figure 27 for the inlet, high-pressure, and low-pressure ports. These measurements were made at the second probe position using the 18-in. rotor with the 0.25-in.-wide passages, at $\epsilon = 0.6$, and $\delta_p = \delta_w = 0.010$ in. The inlet and high-pressure ports are quite uniform, but the low-pressure port is definitely not. The major difference between these ports is that leakage is directed out of the inlet and high-pressure ports, but into the low-pressure port. Presumably the leakage jet entering the low-pressure port can be sufficiently strong to perturb the flow. Since the centerline velocity is greater than the average velocity for the low-pressure port, use of the centerline velocity to calculate the low-pressure port stagnation pressure (via a mixing calculation) would be inaccurate. Instead, the radial distribution of velocity was measured in the low-pressure port on each run using a total pressure rake. This distribution was then used to generate a nonuniformity factor, which was included in the mixing calculation.

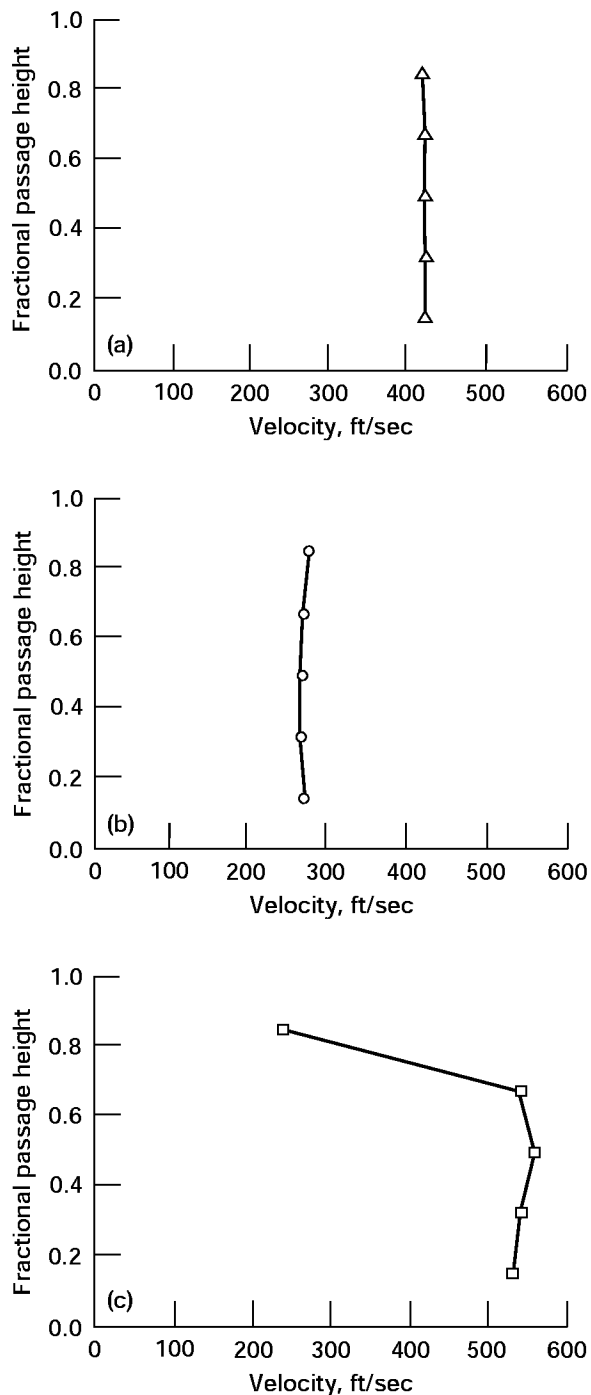


Figure 27.—Radial velocity distributions for the (a) inlet port, (b) high-pressure outlet port, and (c) low-pressure outlet port at $\varepsilon = 0.6$. Measurements were made using the 18-in. rotor with 0.25-in. passage width at the second circumferential probe position. The gap setting was 0.010 in.

If the leakage flow is perturbing the velocity distribution in the low-pressure port, then changing the gap, and hence the amount of leakage, should affect the distribution. That it does is shown by the data in figure 28, for the 9-in. rotor. Drawn in figure 28 are three radial velocity profiles, each taken with the port gap equal to the wall gap, but with three different gap settings. There are two effects. First, as the leakage gap and flow increased, the core flow was confined to a narrower region, and so its velocity increased. Secondly, the highest leakage caused the distribution to become asymmetrical.

Inlet Port Flow Angles

It was stated in the discussion of the work done on the entering flow that the angle of the flow in the inlet port, α , was important in determining the amount of work done. Figure 29 shows the flow angle measured in the inlet port for runs made during the statistical experiment with the 9-in. rotor and 0.54-in.-wide passages at values of $\varepsilon = 0.4, 0.6$, and 0.8 , and for equal port and wall gap settings of $\delta = 0.005$ and 0.0015 in. The wall angle at the leading edge of the port was -32° (see fig. 7), and the duct angle was 36° . The data have been extrapolated to these values at the appropriate end of the port. The most striking observation is that the flow in the whole port seems to have been affected by the inlet rounding, so that all of the flow was at a lower angle than the duct angle. Secondly, it is seen that the flow angle for the case of $\delta = 0.015$ in. seemed to be fairly independent of the expansion ratio, whereas for the case of $\delta = 0.005$ in., the flow angle decreased as the expansion ratio got closer to unity.

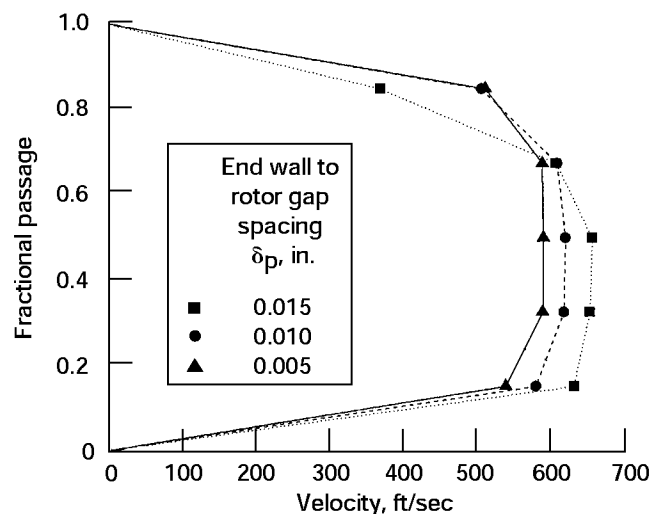


Figure 28.—Radial velocity distributions in the low-pressure outlet port using the 9-in. rotor with 0.54-in.-wide passages and $\delta_p = \delta_w = 0.005, 0.010$, and 0.015 in.

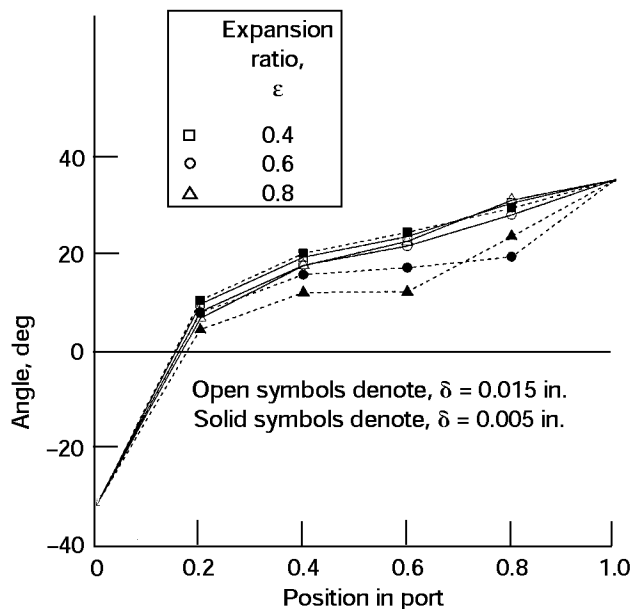


Figure 29.—Measured flow angles in the inlet port for the 9-in. rotor with 0.54-in.-wide passages and $\delta = \delta_p = \delta_w$.

Port Pressures

In making calculations of wave rotor performance, it is frequently assumed that the appropriate boundary conditions are (1) constant stagnation pressure for the inlet port, and (2) constant static pressure for the outlet ports. This is only approximately born out experimentally. In the present experiment, the stagnation pressure in the inlet port was measured 0.85 in. upstream of the rotor and was constant to within about ± 2 percent justifying the use of a constant stagnation pressure boundary condition. The static pressure in the high-pressure port, measured 0.50 in. downstream of the rotor, rose gradually from leading edge to trailing edge, by an amount varying between 2 and 12 percent, depending on conditions. Thus an assumption of constant static pressure is approximately true. In the experiments of Kentfield (1969), the low-pressure port showed a greater variation than the high-pressure port. Along the low-pressure port, Kentfield (1969) found that the static pressure gradually increased, with the final pressure being about 15 percent above the initial value. Results from the present experiment are given in figure 30, again measured 0.50 in. downstream of the rotor. The trend observed by Kentfield is seen here also, but the magnitude is somewhat smaller. The largest increase in static pressure occurs for $\epsilon = 0.4$ and is about 10 percent.

Inlet Pressure Variation

The results of the inlet pressure variation tests, again plotted as measured values of P_{hi}/P_{in} versus P_{lo}/P_{in} , are given in figure 31. The upper set of measurements were made with the 9-in. rotor with a 0.25-in. passage width. The top curve was part

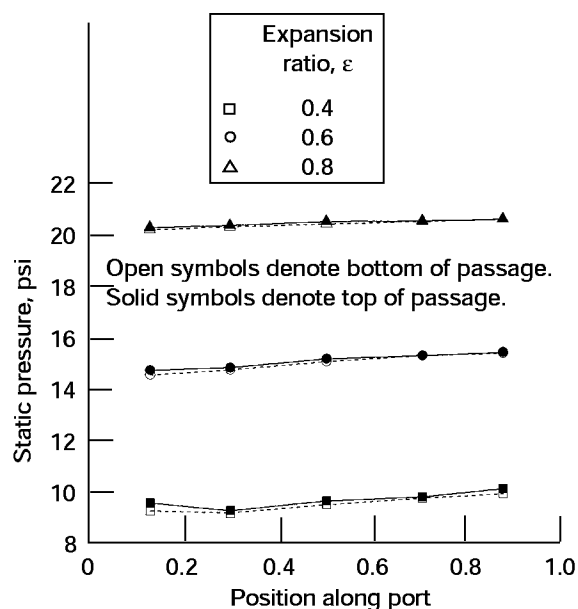


Figure 30.—Static pressure distributions in the low-pressure port. These data were taken with the 9-in. rotor with 0.54-in.-wide passages and $\delta_p = \delta_w = 0.005$ in.

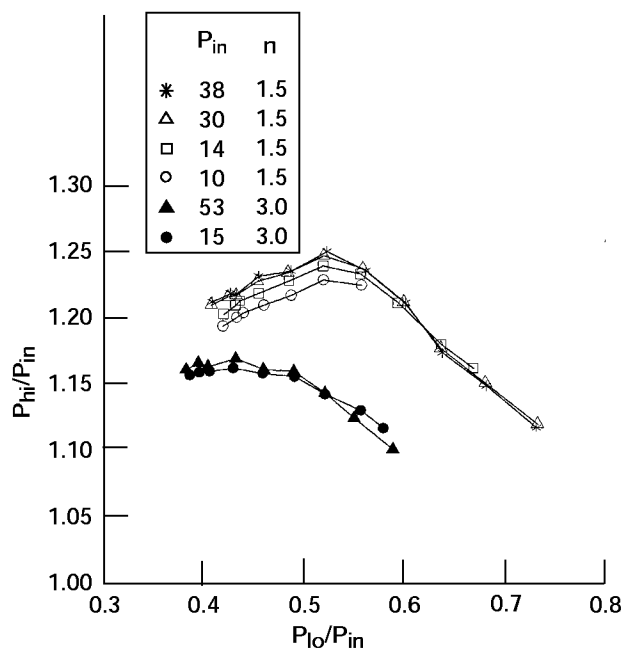


Figure 31.—Observed variations in flow divider performance with changes in inlet stagnation pressure. The measurements were made using the 9-in. rotor with 0.25-in. wide passages at $n = 1.5$ and using the 18-in. rotor with 0.54-in.-wide passages at $n = 3$.

of the statistical experiment. The curves for $n = 3$ were also part of the statistical series but were made with the 18-in. rotor with the 0.54-in. passage width. Inlet pressure variation does play a role in performance but not a very strong one. It was hoped that plotting efficiency against the inverse of the square root of pressure and the inverse of pressure raised to the 0.2 power might give an indication of turbulent or laminar flow. However, the range covered did not permit a determination as to whether the flow was laminar or turbulent. Although the increases in pressure from 10 to 14 psi and from 14 to 30 psi improved performance, the increase from 30 to 38 psi did not. The Reynolds number of the flow in a passage when open to the low-pressure port based on the length of the passage and the axial velocity in the passage was about $3 \cdot 10^6$ at $P_{in} = 38$ psi for the 9-in. rotor. It is possible that the boundary layer was becoming turbulent for this run, but was laminar for the other runs, so that the run at $P = 38$ psi would have had an increase in performance had it been laminar, but did not because of extra friction due to being turbulent. Similarly, one would expect that the large pressure increase from 15 to 53 psi with the 18-in. rotor would have increased performance. The Reynolds number for the run at $P = 53$ psi was about $7 \cdot 10^6$ whereas that for the run at $P = 15$ psi was about $2 \cdot 10^6$. Thus it is possible that the high-pressure run was turbulent, but the low-pressure run was laminar, with the result that these two runs had virtually identical performance.

Brush Seal Tests

The results from the brush seal tests are shown in figure 32, in which the relative efficiency calculated as described in the discussion of losses, is plotted against the leakage parameter. The tests with the brush seal were made with the 9-in. rotor with 0.54-in.-wide passages. Plotted in figure 32 are results with the brush seals from tests at three values of leakage parameter, corresponding to $\delta_p = \delta_w = 0.005, 0.010$, and 0.015 in., for $\varepsilon = 0.6$. For comparison, results without the brush seals with the same rotor from the statistical experiment plus some extra runs are shown. The runs from the statistical experiment are runs 24 to 27. In addition, runs were made at equal port and wall gaps with $\delta = 0.005, 0.010$, and 0.015 -in. The results are remarkably close to a straight line and show that the brush seals do give a significant improvement in performance particularly at large values of leakage parameter. If radial leakage were the only leakage important, and assuming that the brush seals were fully effective in stopping the leakage, there would be no dependence of efficiency on leakage parameter with the brush seals in place. That there is a dependence of efficiency on leakage parameter with the brush seals indicates that circumferential leakage is also important. Circumferential leakage is most easily reduced by reducing the leakage gap, which, of course, also reduces the radial leakage. Thus if the leakage parameter can be made equal to or lower than 0.005, in keeping with the values used by Hoerler, Kentfield, and Thayer, leakage should

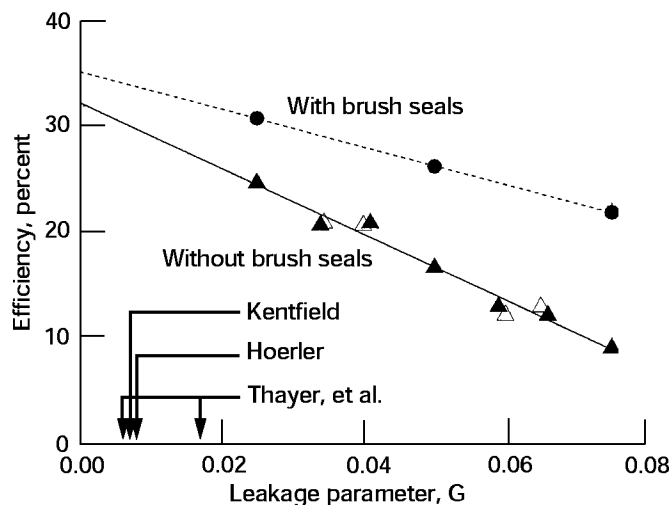


Figure 32.—Relative flow divider efficiency at $\varepsilon = 0.6$ versus leakage parameter with and without brush seals. These data were taken with the 9-in. rotor with 0.54-in.-wide passages.

have little effect on efficiency and the use of brush seals gives little advantage. If larger values of leakage parameter are unavoidable, brush seals can play a role in suppressing leakage.

Inlet Port Leading Edge Rounding

The results of the tests in which the radius of the leading edge rounding was varied are shown in figure 33, plotted as P_{hi}/P_{in} versus P_{lo}/P_{in} . Two runs were made at each value of rounding, one with the sliver in the high-pressure port designed to give the same delay in port opening time as the rounded insert generated in the inlet port, and one with the sliver for the next smallest radius, providing even more delay in opening the high-pressure port. In figure 33, the runs with the increased high-pressure port delay are plotted with a solid symbol and the runs with the designed delay are plotted with an open symbol. The results show that the increased delay provided better performance in all cases. The performance seemed to decrease as the radius was reduced. However, the inlet port angles changed with the rounding, and hence the work, and compression provided by work also changed. The inlet port flow angles for $\varepsilon = 0.33$ are shown in figure 34. As the rounding radius decreases, the flow more nearly approaches the duct angle. The flow angle at the leading edge of the duct, which has the largest effect on the power input, cannot be determined from these results. In these tests, unlike the statistical series, in which the rounding was truncated at -32° , the rounding was not truncated. In principle then, the flow could go around the corner to an angle of -90° . In practice, it probably separates at some angle greater than -90° , resulting in an effective truncation. The results of figure 34 suggest, but do not prove, that this effective truncation angle increases as the radius of rounding is reduced. If this is the case, the reduced performance as the rounding radius decreases

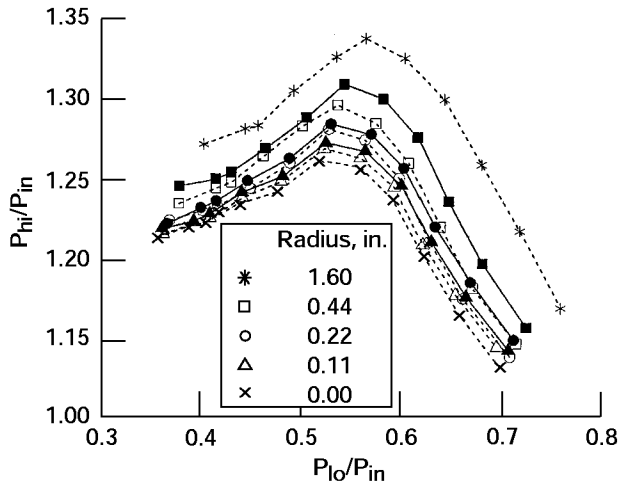


Figure 33.—Flow divider performance using the 9-in. rotor with 0.54-in.-wide passages showing the effect of changing the radius of the rounding of the leading-edge of the inlet port. Solid symbols denote runs whose high-pressure port is delayed, relative to runs denoted by open symbols.

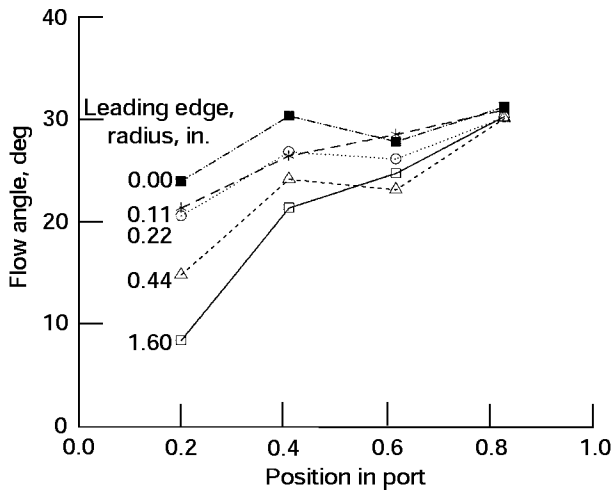


Figure 34.—Inlet port flow angles as a function of position in the port showing the effect of changing the radius of the leading-edge rounding at $\varepsilon = 0.33$. The measurements were made with the 9-in. rotor with 0.54-in.-wide passages and $\delta_p = \delta_w = 0.005$ in.

may simply be a consequence of a smaller amount of work being done on the air as the radius decreases. It may also be a consequence of mistiming as a result of the delayed opening of the inlet port as the radius is reduced.

Motor Power

Measurements of the electric power supplied to the motor which turns the rotor were made towards the end of the test series. Some of this power is used in overcoming the mechanical friction of turning the rotor. This friction power was

measured by operating the rotor at speed but without flow. The friction power was subtracted from the measured values to give the net power put into the airflow. This net power is shown in figure 35(a) plotted against expansion ratio for a run with the 9-in. rotor at equal port and gap settings of 0.005 in. and the original port geometry of figure 7. Also shown are values of power calculated using equation (13), and by using the overall stagnation temperature rise (eq. (11)), using values of T_{hi} and T_{lo} measured at the downstream orifices multiplied by the measured mass flow and specific heat. The downstream measurements of stagnation temperature are not considered very reliable, so the power calculated from them will not be either. Nevertheless, the results are in reasonable agreement, and show the same trend with expansion ratio. A similar plot is shown in

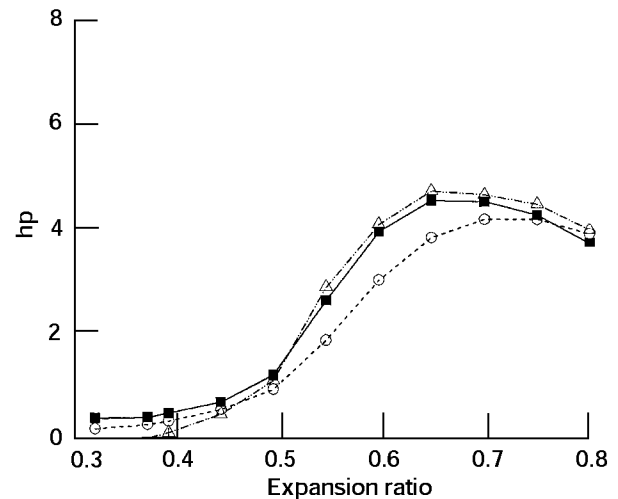
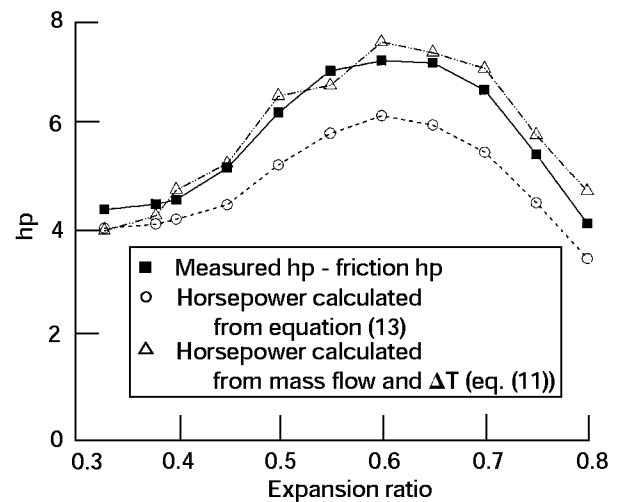


Figure 35.—Comparison of measured power supplied to the electric motor used to drive the rotor, calculated power input to the gas using equation (13), and power calculated from the stagnation temperature rise. (a) 9-in. rotor with standard inlet and (b) 9-in. rotor with leading edge rounding $R = 0$.

figure 35(b), but for the last run of the set of runs in which the radius of the leading edge rounding was changed, namely the run with zero radius. At an expansion ratio of 0.33, the flow is very close to design conditions, and the power into the flow should be very low as was observed. In making these calculations, a value was needed for the flow angle at the leading edge of the port. This was obtained by extrapolating back from the first and second measured flow angles to the port leading edge, assuming the same slope of angle with position.

Evaluation of the Results

Statistical Experiment

At each value of expansion ratio, values of P_{hi}/P_{in} and P_{lo}/P_{in} were used to calculate an efficiency for each run, which was entered into the statistical program RS/Explore as the response, or dependent variable. Values of τ , F_L or F_T , G_p , and G_w for each run were entered as the variables. In principle, this should have been done for all 27 runs. However, as explained in the discussion of the results of the tests in which inlet pressure was varied, there was reason to suspect that the two high-pressure runs (6 and 22) were turbulent, whereas the other runs were laminar. Consequently these two high-pressure runs were omitted from the evaluation with a laminar friction factor. Using the remaining runs, the program calculated those values of the coefficients b_o , b_i , and b_{ii} , in the four variable equivalent of equation (35), namely,

$$\eta = b_o + b_1\tau + b_2F + b_3G_p + b_4G_w + b_{11}\tau^2 + b_{22}F^2 + b_{33}G_p^2 + b_{44}G_w^2 + b_{12}\tau F + b_{13}\tau G_p + b_{14}\tau G_w + b_{23}FG_p + b_{24}FG_w + b_{34}G_p G_w \quad (36)$$

which gave the best fit of equation (36) to the data, with confidence limits as to whether the term should be in the model. Terms with confidence less than 90 percent were dropped, and the coefficients recalculated. The value of b_o is obviously the predicted efficiency with $\tau = F = G_p = G_w = 0$, i.e., the maximum efficiency. It will be equal to the ideal efficiency at the design conditions $\epsilon = 0.33$ at $\beta = 0.37$. Away from these conditions, the maximum efficiency has the same geometry as that of the design: the ideal efficiency is calculated assuming the geometry varies so as to be correct at each condition calculated. What value is obtained for b_o depends on what values of P_{hi}/P_{in} , P_{lo}/P_{in} , F , and f were used. Results are shown in figure 36, using the laminar friction factor F_L . A calculation of the maximum efficiency as a function of expansion ratio made with the CFD code of

Paxson (1995), calculated in the relative frame, is also included in figure 36.

There are three different values of b_o . The first, denoted "uncorrected efficiency," was obtained by inserting the measured absolute values of P_{in} , P_{hi} , and P_{lo} into equation (1) to calculate efficiency. Since this efficiency will contain a pressure change from the flat plate compression, it should not agree with the calculated efficiency which has only a wave rotor contribution. As seen in figure 35, more power is put into the flow as the expansion ratio tends toward unity, so it is to be expected that the uncorrected efficiency will increase as the expansion ratio increases. This is in fact seen. Indeed the uncorrected efficiency reaches unreasonably high values. It is concluded that the uncorrected efficiency is not appropriate for determining wave rotor performance. The second efficiency, denoted "corrected efficiency ($f = 0$)," was obtained by using Pr_{in} , Pr_{hi} , and Pr_{lo} calculated as described in the section on loss summary, but with $f = 0$. This is an even worse fit to the calculated efficiency, showing that this description of the losses is not valid. Finally, the corrected efficiency again used Pr_{in} , Pr_{hi} , and Pr_{lo} , but with the value of f adjusted so that the value of b_o agreed with the calculated maximum efficiency. In effect then, the experiment has been used to determine the value of f . The resulting values of f are plotted in figure 37.

The abscissa in figure 37 is the Mach number at the leading edge of the port averaged over all 25 runs. Since this varied approximately over a range of ± 0.1 , it is not a very accurate quantity. It is used, however, since values of f derived from the data of Lieblein (1965) increase with Mach number, and so it is reasonable to expect that the present results should also. The values $f = 0.6$ and 1.5 , corresponding to the limits of the data of Emmert (1950) are also plotted. No Mach number was given for

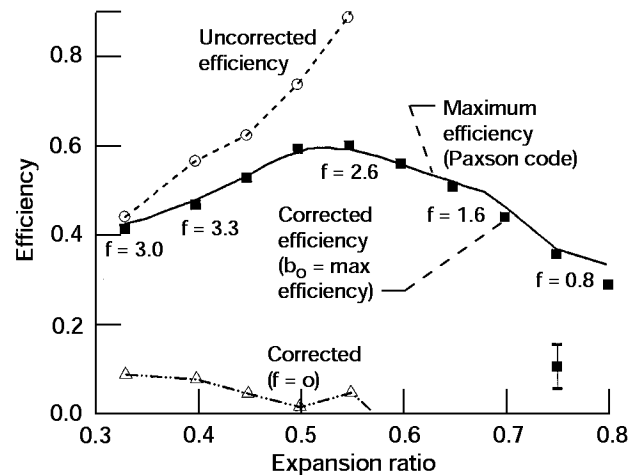


Figure 36.—Values of b_o versus expansion ratio obtained assuming a laminar friction factor, and uncorrected efficiency, efficiency corrected with $f = 0$, and efficiency with f adjusted to make b_o equal to the maximum efficiency. The maximum efficiency was calculated with the CFD code of Paxson (1995).

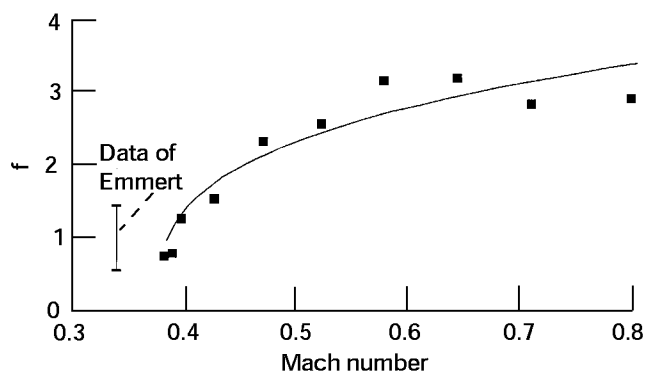


Figure 37.—Values of f ($K/\sin^3(i)$) derived from the experiment versus inlet Mach number, and values that fit the data of Emmert (1950).

these data, and they were arbitrarily plotted at Mach number $= 0.34$. The values of f determined from the present experiment are in reasonable agreement with the data of Emmert (1950) and increase with Mach number, as do values of f derived from the data of Lieblein (1965), though the present results increase far less steeply than Lieblein's data. Thus the values of f obtained from the results seem to be in line with previous determinations, although possibly somewhat low. It is concluded that the incidence loss can be an important loss for a wave rotor and must be taken into account. How important it is will depend on the inlet duct design. A design with no leading edge rounding would be preferable from the point of view of incidence losses, but will have vortex shedding losses (Keller, 1984). An optimum design would minimize the sum of incidence and vortex shedding losses.

Although, for the reasons stated, it was believed that the flow was laminar and the evaluation was repeated using all 27 runs and the turbulent friction factor, F_T . The values of f required to make b_0 agree with the calculated ideal efficiency were about 50 percent higher than those required with the laminar friction factor.

At each value of expansion ratio, the model best fitting the data corrected with the adjusted value of f is given in table V, assuming a laminar friction factor. If no value is given for a

coefficient, then that term has been dropped from the model. The values of f are also given in table V. It will be seen that, for expansion ratios between 0.33 and 0.6, a single model can be fitted to the data, namely

$$\eta = b_0 + b_1\tau + b_2F_L + b_3G_p + b_4G_w + b_{11}\tau^2 + b_{12}\tau F_L \quad (37)$$

The values of the coefficients b_i and b_{ii} at each expansion ratio are not very different from their averages over the six expansion ratios 0.33 to 0.6. The averages are also listed in table V together with their standard deviation. The fact that the coefficients do not change much with expansion ratio suggests that this formulation is reasonably correct. The model is slightly different for the higher expansion ratios, but the results, particularly for b_1 and b_2 , are less reliable since the runs with $n = 3$ could not be made for $\epsilon = 0.75$ and 0.8 , and only partially for $\epsilon = 0.7$. However, higher pressure ratios are generated for expansion ratios below 0.6, so this is the region of greater interest.

The model for expansion ratios less than 0.6, i.e., equation (37) and table V, is surprisingly simple. In particular, it confirms the linear dependence of efficiency on the rotor to end-wall spacing seen in figure 32. However, it indicates that the port leakage gap has a larger effect than the wall gap. Using the average values of the coefficients b_3 and b_4 , the loss in efficiency due to leakage is

$$\Delta\eta = -4.03G_p - 1.35G_w \quad (38)$$

Inserting the expressions for G_p and G_w from equations (32) and (33)

$$\Delta\eta = -2.3(1.24\delta_p + 0.76\delta_w)/H \quad (39)$$

which indicates that according to the experiment, a better expression for the total leakage parameter would be

TABLE V.—VALUES OF THE CONSTANTS IN EQUATION (37)

ϵ	0.33	0.4	0.45	0.5	0.55	0.6	0.65	0.7	0.75	0.8	Average, $\epsilon = 0.33-0.6$	
											b_i	Standard deviation
b_0	0.413	0.467	0.527	0.591	0.598	0.557	0.504	0.436	0.352	0.283	-----	-----
b_1	-0.802	-0.892	-0.944	-1.123	-1.036	-0.811	-0.620	-0.402	-1.417	-1.856	-0.935	0.13
b_2	-1.132	-1.299	-1.456	-1.638	-1.639	-1.100	-1.167	-0.795	-1.067	-0.972	-1.377	0.24
b_3	-2.286	-2.985	-3.563	-4.278	-4.848	-5.262	-5.017	-8.026	-4.533	-4.290	-4.034	1.12
b_4	-0.914	-1.130	-1.271	-1.409	-1.282	-1.794	-1.656	-1.711	-1.785	-1.532	-1.351	0.30
b_{12}	2.94	3.513	3.796	4.434	4.610	2.205	3.079	2.204	11.327	13.377	3.859	0.68
b_{11}	0.545	0.543	0.502	0.610	0.317	0.578	-----	-----	-----	-----	0.516	0.10
b_{33}	-----	-----	-----	-----	-----	-----	-----	5.235	-----	-----	-----	-----
f	3.0	2.92	3.28	3.24	2.64	2.4	1.6	1.32	0.84	0.8	-----	-----

$$G = (1.24 \delta_p + 0.76 \delta_w) / H \quad (40)$$

In figure 32, the results were plotted using both the original total leakage parameter of equation (34) (the solid triangles) and the experimental total leakage parameter above, that is, equation (40) (open triangles) together with a linear least squares fit. Both the original figure leakage parameter and the experimental leakage parameter show a linear relationship between efficiency and leakage parameter; indeed the same least squares line fits both. Thus, there is little to choose between them. The experimental total leakage parameter gives more weight to the port gap spacing than does the original parameter implying that a larger gap could be used for the wall gap spacing than for the port gap spacing should there be any advantage to doing so.

Efficiency Predictions

The empirical model of wave rotor efficiency determined above can be used to optimize efficiency for a specific wave rotor. It will be assumed that the total leakage parameter can be made less than 0.005, such that leakage can be ignored. The terms involving b_3 and b_4 can then be dropped from the model so that the efficiency is a function of opening time and friction factor only. Contours of constant efficiency calculated this way for a value of $\varepsilon = 0.6$ plotted against τ and F_L are given in figure 37. Also shown is a shaded region within which the experiment was conducted. The upper and lower boundaries of this region are curves called rotor loci defined by constant values of rotor diameter and length and passage height, but varying passage width. The opening time is given approximately by

$$\tau = 2nB/D \quad (41)$$

and the friction factor F_L is given by equation (7). Inserting values of velocity and kinematic viscosity into equation (7) leads to (with L and D measured in inches)

$$F_L = 0.016\sqrt{L}/D_h \quad (42)$$

where

$$D_h = 2BH/(B + H) \quad (43)$$

Thus with D , L , and H all given, each value of B determines a value of τ and F_L , and hence a point on the rotor locus. Small values of B correspond to small opening times and large friction factors whereas large values of B give large opening times and small friction factors. The optimum value of B corresponds to the point where the rotor locus is tangent to the maximum efficiency contour that it can touch, i.e., at $\tau = 0.14$, $F_L = 0.12$ for the 9-in.-long rotor, giving an optimum passage

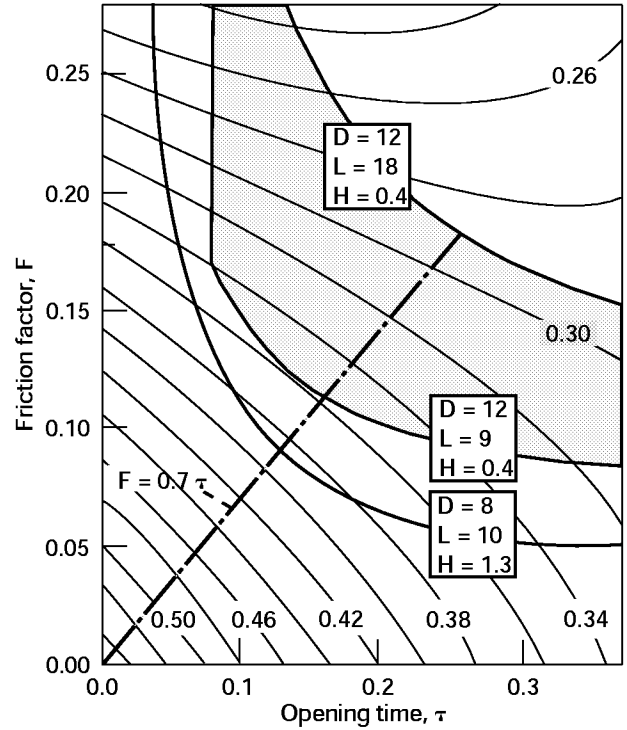


Figure 38.—Predicted contours of relative flow divider efficiency at $\varepsilon = 0.6$, versus opening time and friction factor, assuming no leakage. Also shown are loci of different rotors as the passage width is changed. The experiment was performed within the shaded region.

width of 0.6 in. Also plotted in figure 38 is the rotor locus for a planned rotor with $D = 8$ in., $L = 10$ in., and $H = 1.3$ in. For this rotor, the optimum passage width is 0.52 in. and the rotor should be more efficient than the 9-in. experimental rotor. Approximately, the points of maximum efficiency lie along the line defined by

$$F_L = 0.7\tau \quad (44)$$

The contour plot shows that the maximum efficiency is at the origin, that is, as small a value of friction factor and opening time as possible. This may not be the case in reality for two reasons. First, the model is strictly valid only in the space covered by the experiment which was the region $\tau = 0.085$ to 0.37 , $F_L = 0.09$ to 0.22 . The origin is outside this region and extrapolation of the model to the origin may give erroneous results. Secondly, the results have been referred to the relative frame. As one gets closer to the origin, the rotor length gets smaller and the rotor speed goes up. This can result in the absolute performance being significantly below the relative performance so that a longer, slower rotor may have better performance. Such an effect was found for four-port wave rotors in an optimization study (Wilson and Paxson, 1996).

Conclusions

Operation of a three-port wave rotor has shown that, at a constant value of $\beta = 0.37$, the maximum pressure ratio occurs at an expansion ratio 0.55, and the maximum efficiency at an expansion ratio of 0.65. These expansion ratios are significantly higher than the lowest possible expansion ratio. The loss of efficiency in a wave rotor due to leakage has been demonstrated experimentally to be linear in the end wall to rotor gap spacing. Values of the leakage parameter $G = 2\delta/H$ less than 0.005 are required for good efficiency.

Analysis of the data has indicated that, in addition to losses due to finite opening time, friction, and leakage there are stagnation pressure losses dependent on angle of incidence of the entry flow, and also stagnation pressure gains caused by work input to the gas from the rotor. A simple empirical model was found to fit the dependence of the relative efficiency on opening time, friction, and leakage and used to predict that maximum efficiency will be obtained by designing such that friction and opening time are minimized, with the friction factor equal to seven tenths of the opening time. A model of the incidence losses gave losses in reasonable agreement with limited prior data. The experiment showed that the incidence

losses increase with the inlet Mach number. Incidence losses can be significant and must be taken into account in designing inlet ports.

Use of brush seals was effective in increasing efficiency at large values of leakage parameter, but only gave a small increase in efficiency at small values of leakage parameter. Reducing the radius of the rounding on the leading edge of the inlet port reduced performance, presumably because the work input to the gas decreased with the decreasing radius.

Acknowledgments

The author is grateful to D. Paxson and G. Welch for many fruitful discussions. Special thanks go to C. Horn III, T.J. Doerberling, L.J. Bellisario, and P. Adams, whose careful work in the laboratory made this work possible, to D. Fronek for taking care of all the details of instrumentation, and H. Weaver for operational support.

In addition, thanks are due to all the people who contributed to the design and fabrication effort led by L. Stokley. R.C. Hendricks and T. Wu suggested the use of brush seals and designed and procured them for this application.

Appendix A

Experimental Data for Expansion Ratio = 0.33

Run number	Reading number	Parameters					Measured data			Derived data		
		τ	F_L	F_T	G_p	G_w	P_{hi}/P_{in}	P_{lo}/P_{in}	m, lb/sec	η , uncorrected	η_{CORR} , laminar (P=3.0)	η_{CORR} , turbulent (P=5.2)
1	595	0.0846	0.2168	0.9081	0.0766	0.1338	1.1164	0.3812	1.012	0.0779	0.0866	0.0940
2	709	0.1695	0.2228	0.9182	0.0536	0.1338	1.1149	0.3553	0.526	0.0724	0.0890	0.1021
3	738	0.1694	0.2263	0.9238	0.1148	0.1338	1.0676	0.3517	0.519	0.0429	0.0577	0.0699
4	891	0.1693	0.2172	0.9088	0.0766	0.0669	1.1203	0.3792	0.544	0.0801	0.1003	0.1155
5	916	0.1691	0.2287	0.9277	0.0766	0.2007	1.0873	0.3447	0.508	0.0542	0.0696	0.0819
6	1278	0.0847	0.1280	0.4853	0.0766	0.1338	1.2004	0.4345	1.2933	0.1485	0.1523	0.1757
7	973	0.0847	0.1456	0.5110	0.0766	0.0669	1.2129	0.4330	1.055	0.1566	0.1635	0.2019
8	1037	0.0847	0.1519	0.5197	0.0766	0.2007	1.1850	0.4031	1.001	0.1276	0.1306	0.1661
9	1087	0.0846	0.1458	0.5113	0.0383	0.1338	1.2390	0.4187	1.052	0.1683	0.1719	0.2089
10	1137	0.0846	0.1522	0.5201	0.1148	0.1338	1.1727	0.4139	1.032	0.1228	0.1267	0.1620
11	1429	0.1826	0.1345	0.5897	0.0766	0.1338	1.1867	0.4111	1.115	0.1312	0.1386	0.1532
12	1488	0.1826	0.1306	0.5828	0.0383	0.0669	1.2269	0.4274	1.164	0.1639	0.1762	0.1929
13	1539	0.1828	0.1354	0.5914	0.1148	0.0669	1.1572	0.4337	1.130	0.1178	0.1291	0.1446
14	1639	0.1828	0.1386	0.5969	0.1148	0.2007	1.1279	0.4101	1.103	0.0914	0.1002	0.1145
15	1689	0.1823	0.1362	0.5927	0.0383	0.2007	1.1953	0.3979	1.111	0.1327	0.1418	0.1571
16	1740	0.1827	0.1350	0.5905	0.0766	0.1338	1.1816	0.4072	1.114	0.1267	0.1359	0.1511
17	1812	0.3653	0.1491	0.6145	0.0766	0.0669	1.1631	0.3574	0.548	0.1017	0.1158	0.1303
18	1886	0.3655	0.1368	0.5938	0.0766	0.2007	1.1327	0.3840	0.530	0.0890	0.1031	0.1171
19	1899	0.3653	0.1341	0.5891	0.0383	0.1338	1.1822	0.3882	0.549	0.1215	0.1376	0.1529
20	1942	0.3648	0.1333	0.5877	0.1148	0.1338	1.1212	0.4069	0.546	0.0861	0.1020	0.1175
21	2026	0.3662	0.1916	0.6794	0.0766	0.1338	1.1454	0.3944	0.276	0.0995	0.1149	0.1300
22	1985	0.3656	0.1020	0.5280	0.0766	0.1338	1.1532	0.3981	0.933	0.1055	0.1215	0.1361
23	1589	0.1828	0.1350	0.5906	0.0766	0.1338	1.1759	0.4089	1.122	0.1234	0.1334	0.1486
24	2062	0.1824	0.1014	0.3475	0.0383	0.1338	1.2504	0.4197	1.083	0.1763	0.1716	0.2109
25	2115	0.1830	0.0995	0.3449	0.1148	0.1338	1.1931	0.4452	1.086	0.1472	0.1403	0.1803
26	2322	0.1824	0.1011	0.3471	0.0766	0.0669	1.2409	0.4281	1.099	0.1736	0.1738	0.2133
27	2219	0.1825	0.1029	0.3495	0.0766	0.2007	1.1970	0.4167	1.033	0.1399	0.1326	0.1725

Appendix B

Experimental Data for Expansion Ratio = 0.4

Run number	Reading number	Parameters					Measured data			Derived data		
		τ	F_L	F_T	G_p	G_w	P_{hi}/P_{in}	P_{lo}/P_{in}	m , lb/sec	η , Uncorrected	η_{CORR} , laminar ($P=2.92$)	η_{CORR} , turbulent ($P=5.2$)
1	596	0.0846	0.2130	0.9017	0.0766	0.1338	1.1178	0.4178	0.977	0.0860	0.0924	0.1009
2	710	0.1695	0.2192	0.9121	0.0536	0.1338	1.1188	0.3876	0.517	0.0807	0.0962	0.1107
3	739	0.1694	0.2162	0.9072	0.1148	0.1338	1.0672	0.3977	0.507	0.0475	0.0620	0.0759
4	892	0.1692	0.2087	0.8944	0.0766	0.0669	1.1202	0.4261	0.526	0.0895	0.1093	0.1269
5	915	0.1691	0.2178	0.9098	0.0766	0.2007	1.0902	0.3917	0.497	0.0624	0.0776	0.0918
6	1279	0.0846	0.1271	0.4838	0.0766	0.1338	1.2064	0.4546	1.276	0.1604	0.1607	0.1860
7	974	0.0847	0.1425	0.5065	0.0766	0.0669	1.2223	0.4655	1.044	0.1767	0.1791	0.2221
8	1038	0.0847	0.1482	0.5146	0.0766	0.2007	1.1914	0.4320	0.988	0.1413	0.1386	0.1784
9	1088	0.0846	0.1425	0.5065	0.0383	0.1338	1.2458	0.4557	1.036	0.1892	0.1880	0.2318
10	1138	0.0846	0.1467	0.5124	0.1148	0.1338	1.1783	0.4498	1.016	0.1381	0.1362	0.1759
11	1430	0.1824	0.1313	0.5841	0.0766	0.1338	1.1965	0.4417	1.090	0.1483	0.1527	0.1695
12	1489	0.1825	0.1273	0.5769	0.0383	0.0669	1.2384	0.4674	1.136	0.1894	0.1987	0.2187
13	1540	0.1828	0.1325	0.5862	0.1148	0.0669	1.1634	0.4480	1.108	0.1266	0.1334	0.1500
14	1640	0.1828	0.1354	0.5912	0.1148	0.2007	1.1325	0.4265	1.077	0.0983	0.1041	0.1196
15	1690	0.1824	0.1320	0.5854	0.0383	0.2007	1.2065	0.4351	1.096	0.1529	0.1597	0.1777
16	1741	0.1827	0.1312	0.5839	0.0766	0.1338	1.1889	0.4405	1.095	0.1425	0.1490	0.1665
17	1813	0.3653	0.1383	0.5964	0.0766	0.0669	1.1638	0.4205	0.532	0.1186	0.1332	0.1509
18	1887	0.3655	0.1380	0.5958	0.0766	0.2007	1.1344	0.9369	0.518	0.0929	0.1052	0.1198
19	1900	0.3652	0.1335	0.5880	0.0383	0.1338	1.1863	0.4133	0.535	0.1317	0.1463	0.1632
20	1943	0.3649	0.1366	0.5934	0.1148	0.1338	1.1224	0.4172	0.521	0.0891	0.1025	0.1185
21	2027	0.3671	0.1392	0.6803	0.0766	0.1338	1.1489	0.4158	0.265	0.1072	0.1208	0.1370
22	1986	0.3656	0.1034	0.5309	0.0766	0.1338	1.1544	0.4141	0.899	0.1105	0.1244	0.1398
23	1590	0.1828	0.1317	0.5848	0.0766	0.1338	1.1838	0.4399	1.099	0.1387	0.1462	0.1635
24	2063	0.1824	0.0960	0.3399	0.0383	0.1338	1.2597	0.4583	1.085	0.2004	0.1891	0.2362
25	2116	0.1830	0.0982	0.3430	0.1148	0.1338	1.1974	0.4545	1.073	0.1537	0.1408	0.1845
26	2323	0.1824	0.0961	0.3402	0.0766	0.0669	1.2512	0.4650	1.095	0.1976	0.1904	0.2372
27	2220	0.1825	0.1001	0.3457	0.0766	0.2007	1.2000	0.4345	1.035	0.1480	0.1369	0.1812

Appendix C

Experimental Data for Expansion Ratio = 0.45

Run number	Reading number	Parameters					Measured data			Derived data		
		τ	F_L	F_T	G_p	G_w	P_{hi}/P_{in}	P_{lo}/P_{in}	m, lb/sec	η , uncorrected	η_{CORR} , laminar (P=3,28)	η_{CORR} , turbulent (P=5,2)
1	604	0.0846	0.2162	0.9072	0.0766	0.1338	1.1222	0.4402	0.947	0.0941	0.1001	0.1078
2	707	0.1695	0.2214	0.9157	0.0536	0.1338	1.1228	0.4126	0.500	0.0884	0.1061	0.1191
3	736	0.1693	0.2183	0.9107	0.1148	0.1338	1.070	0.4195	0.488	0.0519	0.0682	0.0804
4	889	0.1692	0.2091	0.8951	0.0766	0.0669	1.1244	0.4530	0.512	0.0988	0.1213	0.1373
5	911	0.1690	0.2201	0.9136	0.0766	0.2007	1.0941	0.4146	0.481	0.0687	0.0859	0.0985
6	1359	0.0845	0.1313	0.4902	0.0766	0.1338	1.2248	0.4783	1.249	0.1844	0.1816	0.2257
7	971	0.0847	0.1443	0.5090	0.0766	0.0669	1.2359	0.4912	1.010	0.1993	0.2004	0.2418
8	1035	0.0847	0.1513	0.5189	0.0766	0.2007	1.2020	0.4531	0.951	0.1566	0.1551	0.1926
9	1085	0.0847	0.1449	0.5099	0.0383	0.1338	1.2565	0.4845	0.991	0.2117	0.2088	0.2517
10	1135	0.0846	0.1490	0.5157	0.1148	0.1338	1.1873	0.4721	0.974	0.1530	0.1509	0.1886
11	1427	0.1826	0.1331	0.5873	0.0766	0.1338	1.2095	0.4673	1.045	0.1679	0.1729	0.1888
12	1486	0.1825	0.1276	0.5775	0.0383	0.0669	1.2592	0.4999	1.099	0.2224	0.2309	0.2502
13	1537	0.1828	0.1327	0.5867	0.1148	0.0669	1.1735	0.4754	1.062	0.1435	0.1512	0.1666
14	1637	0.1828	0.1367	0.5936	0.1148	0.2007	1.1408	0.4508	1.032	0.1106	0.1176	0.1317
15	1687	0.1823	0.1345	0.5897	0.0383	0.2007	1.2226	0.4636	1.041	0.1760	0.1834	0.2002
16	1738	0.1827	0.1328	0.5867	0.0766	0.1338	1.2024	0.4673	1.047	0.1626	0.1696	0.1859
17	1810	0.3652	0.1399	0.5991	0.0766	0.0669	1.1661	0.4448	0.513	0.1276	0.1450	0.1610
18	1852	0.3651	0.1392	0.5979	0.0766	0.2007	1.1411	0.4223	0.498	0.1034	0.1181	0.1313
19	1897	0.3652	0.1346	0.5900	0.0383	0.1338	1.1967	0.4401	0.516	0.1479	0.1653	0.1807
20	1940	0.3651	0.1385	0.5968	0.1148	0.1338	1.1250	0.4423	0.501	0.0967	0.1128	0.1272
21	2024	0.3676	0.1951	0.6843	0.0766	0.1338	1.1509	0.4385	0.257	0.1146	0.1305	0.1448
22	1983	0.3656	0.1038	0.5317	0.0766	0.1338	1.1607	0.4409	0.877	0.1224	0.1391	0.1529
23	1587	0.1828	0.1328	0.5868	0.0766	0.1338	1.1986	0.4675	1.056	0.1598	0.1679	0.1841
24	2058	0.1823	0.0972	0.3417	0.0383	0.1338	1.2773	0.4871	1.034	0.2290	0.2164	0.2626
25	2113	0.1831	0.0992	0.3444	0.1148	0.1338	1.2066	0.4765	1.032	0.1696	0.1577	0.1990
26	2320	0.1824	0.0956	0.3394	0.0766	0.0669	1.2672	0.4950	1.069	0.2259	0.2170	0.2624
27	2217	0.1825	0.1007	0.3465	0.0766	0.2007	1.2081	0.4564	0.998	0.1623	0.1535	0.1952

Appendix D

Experimental Data for Expansion Ratio = 0.5

Run number	Reading number	Parameters					Measured data			Derived data		
		τ	F_L	F_T	G_p	G_w	P_{in}/P_{in}	P_{lo}/P_{in}	m, lb/sec	η , uncorrected	η_{CORR} , laminar (P=3.24)	η_{CORR} , turbulent (P=5.04)
1	597	0.0846	0.2191	0.9119	0.0766	0.1338	1.1208	0.4675	0.917	0.0996	0.1035	0.1114
2	711	0.1695	0.2229	0.9183	0.0536	0.1338	1.1222	0.4412	0.483	0.0943	0.1117	0.1246
3	740	0.1694	0.2207	0.9147	0.1148	0.1338	1.0641	0.4440	0.475	0.0508	0.0663	0.0780
4	893	0.1692	0.2128	0.9014	0.0766	0.0669	1.1156	0.4824	0.488	0.0992	0.1209	0.1368
5	917	0.1691	0.2205	0.9142	0.0766	0.2007	1.0875	0.4400	0.472	0.0681	0.0846	0.0967
6	1280	0.0847	0.1324	0.4919	0.0766	0.1338	1.2215	0.5057	1.203	0.1952	0.1861	0.2122
7	975	0.0847	0.1460	0.5115	0.0766	0.0669	1.2470	0.5216	0.987	0.2253	0.2156	0.2604
8	1039	0.0847	0.1526	0.5206	0.0766	0.2007	1.2037	0.4791	0.937	0.1685	0.1610	0.2011
9	1089	0.0846	0.1458	0.5113	0.0383	0.1338	1.2711	0.5181	0.973	0.2433	0.2301	0.2790
10	1139	0.0846	0.1506	0.5179	0.1148	0.1338	1.1869	0.4954	0.959	0.1621	0.1534	0.1929
11	1431	0.1824	0.1337	0.5883	0.0766	0.1338	1.2095	0.4948	1.018	0.1801	0.1824	0.1993
12	1490	0.1825	0.1301	0.5819	0.0383	0.0669	1.2598	0.5319	1.044	0.2427	0.2472	0.2684
13	1541	0.1829	0.1338	0.5885	0.1148	0.0669	1.1665	0.5007	1.038	0.1473	0.1521	0.1677
14	1641	0.1828	0.1380	0.5958	0.1148	0.2007	1.1339	0.4745	1.004	0.1119	0.1169	0.1309
15	1691	0.1824	0.1356	0.5917	0.0383	0.2007	1.2255	0.4939	1.005	0.1924	0.1967	0.2147
16	1742	0.1827	0.1352	0.5910	0.0766	0.1338	1.1997	0.4936	1.001	0.1716	0.1760	0.1929
17	1814	0.3653	0.1411	0.6011	0.0766	0.0669	1.1582	0.4728	0.495	0.1306	0.1474	0.1631
18	1856	0.3651	0.1409	0.6008	0.0766	0.2007	1.1359	0.4474	0.479	0.1061	0.1199	0.1326
19	1901	0.3652	0.1368	0.5938	0.0383	0.1338	1.1915	0.4664	0.492	0.1540	0.1705	0.1857
20	1944	0.3646	0.1405	0.6001	0.1148	0.1338	1.1170	0.4703	0.482	0.0973	0.1126	0.1266
21	2028	0.3670	0.1985	0.6891	0.0766	0.1338	1.1478	0.4709	0.246	0.1219	0.1371	0.1513
22	1987	0.3657	0.1058	0.5358	0.0766	0.1338	1.1525	0.4686	0.836	0.1248	0.1407	0.1541
23	1591	0.1828	0.1343	0.5894	0.0766	0.1338	1.1959	0.4940	1.022	0.1688	0.1740	0.1907
24	2064	0.1825	0.0976	0.3422	0.0383	0.1338	1.2836	0.5176	1.013	0.2532	0.2313	0.2835
25	2117	0.1829	0.0998	0.3453	0.1148	0.1338	1.2048	0.5015	1.019	0.1794	0.1620	0.2060
26	2324	0.1824	0.0965	0.3406	0.0766	0.0669	1.2720	0.5238	1.044	0.2478	0.2290	0.2779
27	2221	0.1825	0.1014	0.3475	0.0766	0.2007	1.2084	0.4818	0.972	0.1733	0.1597	0.2043

Appendix E

Experimental Data for Expansion Ratio = 0.55

Run number	Reading number	Parameters					Measured data			Derived data		
		τ	F_L	F_T	G_p	G_w	P_{hi}/P_{in}	P_{lo}/P_{in}	m, lb/sec	η , uncorrected	η_{CORR} , laminar (P=2.64)	η_{CORR} , turbulent (P=4.4)
1	607	0.0846	0.2277	0.9261	0.0765	0.1336	1.1165	0.4964	0.856	0.1035	0.1012	0.1105
2	706	0.1695	0.2517	0.9640	0.0536	0.1337	1.1212	0.4729	0.458	0.1013	0.1135	0.1268
3	735	0.1694	0.2258	0.9230	0.1147	0.1336	1.0636	0.4727	0.449	0.0542	0.0649	0.0767
4	888	0.1692	0.2171	0.9086	0.0764	0.0668	1.1180	0.5155	0.466	0.1103	0.1262	0.1427
5	910	0.1690	0.2279	0.9264	0.0764	0.2004	1.0885	0.4696	0.442	0.0742	0.0858	0.0981
6	1275	0.0845	0.1394	0.5022	0.0765	0.1336	1.2347	0.5388	1.117	0.2251	0.1941	0.2251
7	970	0.0847	0.1532	0.5215	0.0765	0.0668	1.2554	0.5562	0.914	0.2555	0.2165	0.2713
8	1034	0.0847	0.1609	0.5317	0.0765	0.2005	1.2123	0.5103	0.868	0.1899	0.1597	0.2068
9	1084	0.0846	0.1541	0.5227	0.0382	0.1337	1.2788	0.5525	0.894	0.2742	0.2325	0.2947
10	1134	0.0846	0.1574	0.5271	0.1147	0.1337	1.1911	0.5254	0.897	0.1791	0.1477	0.1929
11	1426	0.1827	0.1389	0.5974	0.0765	0.1336	1.2174	0.5292	0.941	0.2042	0.1974	0.2175
12	1485	0.1827	0.1345	0.5898	0.0383	0.0668	1.2639	0.5695	0.969	0.2735	0.2656	0.2922
13	1536	0.1828	0.1382	0.5962	0.1147	0.0668	1.1687	0.5332	0.974	0.1626	0.1584	0.1759
14	1636	0.1827	0.1424	0.6034	0.1147	0.2005	1.1378	0.5034	0.952	0.1240	0.1211	0.1362
15	1686	0.1822	0.1418	0.6023	0.0382	0.2005	1.2283	0.5260	0.933	0.2119	0.2063	0.2273
16	1737	0.1827	0.1393	0.5981	0.0765	0.1337	1.2055	0.5284	0.937	0.1933	0.1880	0.2077
17	1840	0.3654	0.1456	0.6087	0.0764	0.0668	1.1546	0.5039	0.466	0.1384	0.1495	0.1657
18	1851	0.3650	0.1461	0.6097	0.0765	0.2005	1.1358	0.4741	0.456	0.1133	0.1225	0.1354
19	1927	0.3654	0.1420	0.6027	0.0383	0.1337	1.1927	0.4981	0.458	0.1679	0.1788	0.1947
20	1970	0.3653	0.1451	0.6079	0.1147	0.1336	1.1141	0.5010	0.455	0.1028	0.1128	0.1270
21	2033	0.3671	0.2252	0.7248	0.0765	0.1336	1.1495	0.5032	0.193	0.1338	0.1435	0.1581
22	1982	0.3650	0.1092	0.5427	0.0765	0.1336	1.1510	0.4995	0.799	0.1338	0.1442	0.1580
23	1586	0.1827	0.1383	0.5964	0.0765	0.1336	1.2026	0.5298	0.957	0.1915	0.1870	0.2062
24	2108	0.1823	0.1015	0.3477	0.0382	0.1336	1.2983	0.5525	0.948	0.2917	0.2412	0.3064
25	2112	0.1831	0.1026	0.3492	0.1147	0.1337	1.2092	0.5307	0.974	0.1978	0.1588	0.2078
26	2319	0.1824	0.1009	0.3469	0.0765	0.0668	1.2838	0.5568	0.974	0.2821	0.2335	0.2911
27	2216	0.1825	0.1056	0.3532	0.0765	0.2005	1.2129	0.5092	0.920	0.1899	0.1551	0.2051

Appendix F

Experimental Data for Expansion Ratio = 0.6

Run number	Reading number	Parameters					Measured data			Derived data		
		τ	F_L	F_T	G_p	G_w	P_{hi}/P_{in}	P_{lo}/P_{in}	m , lb/sec	η , uncorrected	η_{CORR} , laminar ($P=2.4$)	η_{CORR} , turbulent ($P=3.8$)
1	618	0.0876	0.2712	0.9932	0.0756	0.1321	1.1130	0.5328	0.744	0.1108	0.1132	0.1159
2	695	0.1695	0.2724	0.9950	0.0529	0.1321	1.1111	0.5097	0.414	0.1025	0.1119	0.1229
3	764	0.1693	0.2329	0.9345	0.1133	0.1320	1.0564	0.5063	0.419	0.0525	0.0608	0.0704
4	897	0.1692	0.2245	0.9208	0.0755	0.0660	1.1068	0.5512	0.431	0.1104	0.1229	0.1367
5	949	0.1691	0.2338	0.9360	0.0756	0.1982	1.0774	0.4996	0.417	0.0703	0.0793	0.0891
6	1281	0.0847	0.1444	0.5093	0.0757	0.1322	1.2196	0.5739	1.053	0.2336	0.1881	0.2192
7	1008	0.0846	0.1611	0.5320	0.0757	0.0661	1.2507	0.5939	0.850	0.2802	0.2228	0.2809
8	1057	0.0846	0.1685	0.5417	0.0756	0.1983	1.2031	0.5427	0.824	0.1988	0.1560	0.2032
9	1090	0.0846	0.1590	0.5292	0.0378	0.1322	1.2611	0.5896	0.851	0.2872	0.2328	0.3013
10	1140	0.0846	0.1626	0.5341	0.1135	0.1322	1.1823	0.5565	0.855	0.1866	0.1426	0.1861
11	1463	0.1828	0.1444	0.6068	0.0757	0.1323	1.2044	0.5606	0.882	0.2102	0.1983	0.2171
12	1484	0.1827	0.1393	0.5981	0.0378	0.0661	1.2480	0.6076	0.901	0.2892	0.2746	0.3010
13	1559	0.1827	0.1432	0.6048	0.1135	0.0661	1.1592	0.5648	0.913	0.1682	0.1582	0.1739
14	1642	0.1828	0.1471	0.6112	0.1135	0.1984	1.1199	0.5320	0.899	0.1170	0.1099	0.1226
15	1692	0.1823	0.1478	0.6124	0.0378	0.1983	1.2065	0.5585	0.860	0.2110	0.2006	0.2196
16	1760	0.1823	0.1456	0.6088	0.0757	0.1323	1.1903	0.5609	0.868	0.1968	0.1860	0.2041
17	1808	0.3652	0.1493	0.6149	0.0756	0.0660	1.1417	0.5385	0.434	0.1398	0.1478	0.1612
18	1857	0.3651	0.1519	0.6192	0.0757	0.1985	1.1238	0.5041	0.421	0.1121	0.1184	0.1287
19	1915	0.3651	0.1475	0.6119	0.0379	0.1324	1.1805	0.5299	0.426	0.1719	0.1796	0.1926
20	1938	0.3650	0.1507	0.6172	0.1135	0.1322	1.1051	0.5340	0.425	0.1037	0.1107	0.1223
21	2029	0.3664	0.2156	0.7123	0.0756	0.1322	1.1322	0.5342	0.216	0.1293	0.1361	0.1479
22	1988	0.3657	0.1140	0.5520	0.0756	0.1321	1.1312	0.5316	0.740	0.1274	0.1348	0.1454
23	1592	0.1828	0.1432	0.6047	0.0756	0.1322	1.1811	0.5600	0.902	0.1874	0.1778	0.1947
24	2065	0.1825	0.1049	0.3523	0.0378	0.1322	1.2776	0.5867	0.906	0.3013	0.2380	0.3038
25	2155	0.1828	0.1068	0.3548	0.1135	0.1322	1.2013	0.5626	0.924	0.2085	0.1566	0.2036
26	2355	0.1826	0.1059	0.3536	0.0757	0.0661	1.2787	0.5939	0.915	0.3089	0.2411	0.3009
27	2215	0.1826	0.1104	0.3595	0.0757	0.1984	1.2048	0.5381	0.875	0.1979	0.1522	0.1995

Appendix G

Experimental Data for Expansion Ratio = 0.65

Run number	Reading number	Parameters					Measured data			Derived data		
		τ	F_L	F_T	G_p	G_w	P_{hi}/P_{in}	P_{lo}/P_{in}	m, lb/sec	η , uncorrected	η_{CORR} , laminar (P=1.6)	η_{CORR} , turbulent (P=3.2)
1	602	0.0844	0.2551	0.9691	0.0740	0.1293	1.1042	0.5638	0.719	0.1116	0.0941	0.1078
2	713	0.1695	0.2450	0.9537	0.0518	0.1293	1.0968	0.5428	0.403	0.0981	0.0997	0.1128
3	742	0.1693	0.2374	0.9418	0.1106	0.1288	1.0460	0.5397	0.398	0.0470	0.0485	0.0597
4	896	0.1692	0.2315	0.9323	0.0738	0.0644	1.0928	0.5878	0.399	0.1070	0.1100	0.1264
5	920	0.1690	0.2425	0.9497	0.0738	0.1935	1.0679	0.5351	0.385	0.0680	0.0697	0.0814
6	1285	0.0847	0.1539	0.5224	0.0740	0.1293	1.1997	0.6135	0.946	0.2407	0.1607	0.2082
7	980	0.0847	0.1715	0.5455	0.0740	0.0647	1.2249	0.6298	0.775	0.2832	0.1818	0.2664
8	1044	0.0846	0.1813	0.5578	0.0740	0.1939	1.1819	0.5757	0.738	0.1968	0.1201	0.1855
9	1094	0.0846	0.1717	0.5458	0.0370	0.1293	1.2399	0.6254	0.749	0.2966	0.1942	0.2938
10	1144	0.0846	0.1744	0.5492	0.1110	0.1293	1.1684	0.5897	0.783	0.1907	0.1112	0.1724
11	1436	0.1824	0.1517	0.6188	0.0740	0.1293	1.1840	0.5922	0.808	0.2089	0.1822	0.2081
12	1495	0.1825	0.1470	0.6111	0.0370	0.0647	1.2201	0.6463	0.808	0.2930	0.2575	0.2951
13	1546	0.1829	0.1488	0.6141	0.1110	0.0646	1.1410	0.6022	0.834	0.1672	0.1432	0.1644
14	1646	0.1826	0.1556	0.6251	0.1110	0.1939	1.1129	0.5649	0.821	0.1211	0.1022	0.1190
15	1696	0.1823	0.1554	0.6248	0.0370	0.1939	1.1870	0.5929	0.778	0.2125	0.1868	0.2129
16	1747	0.1826	0.1524	0.6200	0.0740	0.1292	1.1657	0.5946	0.787	0.1905	0.1656	0.1896
17	1817	0.3652	0.1542	0.6229	0.0739	0.0646	1.1281	0.5736	0.397	0.1402	0.1393	0.1550
18	1859	0.3651	0.1601	0.6323	0.0740	0.1940	1.1116	0.5386	0.387	0.1112	0.1103	0.1225
19	1904	0.3653	0.1552	0.6245	0.0371	0.1296	1.1657	0.5637	0.386	0.1740	0.1729	0.1883
20	1947	0.3648	0.1593	0.6310	0.1108	0.1291	1.0887	0.5704	0.389	0.0974	0.0966	0.1100
21	2031	0.3682	0.2314	0.7327	0.0738	0.1289	1.1228	0.5724	0.198	0.1341	0.1328	0.1470
22	1990	0.3656	0.1234	0.5697	0.0739	0.1292	1.1173	0.5660	0.682	0.1260	0.1253	0.1379
23	1596	0.1827	0.1506	0.6170	0.0739	0.1292	1.1680	0.5984	0.814	0.1953	0.1702	0.1940
24	2069	0.1823	0.1131	0.3630	0.0370	0.1294	1.2648	0.6205	0.820	0.3199	0.2101	0.3050
25	2122	0.1828	0.1137	0.3638	0.1110	0.1293	1.1915	0.5959	0.849	0.2192	0.1307	0.1956
26	2329	0.1823	0.1131	0.3631	0.0740	0.0647	1.2579	0.6300	0.844	0.3218	0.2083	0.2949
27	2226	0.1825	0.1183	0.3696	0.0740	0.1939	1.1897	0.5710	0.794	0.2020	0.1230	0.1872

Appendix H

Experimental Data for Expansion Ratio = 0.7

Run number	Reading number	Parameters					Measured data			Derived data		
		τ	F_L	F_T	G_p	G_w	P_{hi}/P_{in}	P_{lo}/P_{in}	m , lb/sec	η , uncorrected	η_{CORR} , laminar ($P=1.32$)	η_{CORR} , turbulent ($P=2.2$)
1	599	0.0846	0.2665	0.9862	0.0178	0.323	1.0865	0.6018	0.641	0.1043	0.0805	0.0884
2	---	---	---	---	---	---	---	---	---	---	---	---
3	743	0.1693	0.2471	0.9568	0.0266	0.0323	1.0390	0.5768	0.367	0.0444	0.0425	0.0485
4	895	0.1692	0.2368	0.9408	0.0178	0.0161	1.0795	0.6216	0.371	0.1022	0.1005	0.1096
5	919	0.1690	0.2474	0.9574	0.0178	0.0484	1.0540	0.5727	0.3566	0.0604	0.0586	0.0648
6	1282	0.0847	0.1633	0.5350	0.0178	0.0323	1.1637	0.6494	0.851	0.2241	0.1238	0.1551
7	977	0.0847	0.1824	0.5591	0.0178	0.0161	1.1866	0.6678	0.707	0.2701	0.1446	0.1991
8	1041	0.0846	0.1923	0.5711	0.0178	0.0484	1.1512	0.6089	0.673	0.1825	0.0896	0.1290
9	1091	0.0846	0.1807	0.5570	0.0089	0.0323	1.2039	0.6633	0.667	0.2890	0.1621	0.2249
10	1141	0.0846	0.1875	0.5653	0.0266	0.0323	1.1393	0.6224	0.714	0.1759	0.0793	0.1164
11	1433	0.1825	0.1575	0.6282	0.0178	0.0323	1.1545	0.6252	0.729	0.1959	0.1621	0.1776
12	1492	0.1825	0.1539	0.6224	0.0089	0.0161	1.1838	0.6855	0.717	0.2836	0.2371	0.2609
13	1543	0.1828	0.1577	0.6285	0.0266	0.0161	1.1140	0.6354	0.749	0.1514	0.1202	0.1324
14	1643	0.1826	0.1636	0.6379	0.0266	0.0484	1.0888	0.5997	0.754	0.1063	0.0815	0.0908
15	1693	0.1823	0.1615	0.6345	0.0089	0.0484	1.1570	0.6283	0.703	0.2010	0.1678	0.1832
16	1744	0.1827	0.1578	0.6286	0.0178	0.0323	1.1376	0.6277	0.713	0.1768	0.1448	0.1588
17	1816	0.3652	0.1577	0.6285	0.0178	0.0161	1.1132	0.6066	0.366	0.1373	0.1323	0.1410
18	1858	0.3651	0.1699	0.6475	0.0178	0.0484	1.0936	0.5756	0.353	0.1042	0.0998	0.1064
19	1903	0.3653	0.1587	0.6301	0.0089	0.0323	1.1555	0.5784	0.371	0.1710	0.1665	0.1747
20	1946	0.3645	0.1644	0.6391	0.0266	0.0323	1.0748	0.6001	0.358	0.0901	0.0859	0.0931
21	2030	0.3660	0.2351	0.7374	0.0178	0.0323	1.1073	0.5935	0.189	0.1254	0.1207	0.1283
22	1989	0.3657	0.1280	0.5781	0.0178	0.0323	1.0941	0.6040	0.616	0.1139	0.1093	0.1153
23	1593	0.1827	0.1577	0.6286	0.0178	0.0323	1.1392	0.6289	0.731	0.1796	0.1475	0.1610
24	2066	0.1824	0.1223	0.3746	0.0089	0.0323	1.2273	0.6567	0.731	0.3126	0.1797	0.2396
25	2119	0.1828	0.1211	0.3731	0.0266	0.0323	1.1613	0.6299	0.782	0.2072	0.1008	0.1406
26	2326	0.1824	0.1214	0.3734	0.0178	0.0161	1.2221	0.6672	0.770	0.3172	0.1783	0.2342
27	2223	0.1825	0.1259	0.3789	0.0178	0.0484	1.1601	0.6028	0.732	0.1890	0.0950	0.1334

Appendix I

Experimental Data for Expansion Ratio = 0.75

Run number	Reading number	Parameters					Measured data			Derived data		
		τ	F_L	F_T	G_p	G_w	P_{hi}/P_{in}	P_{lo}/P_{in}	m, lb/sec	η , uncorrected	η_{CORR} , laminar (P=0.84)	η_{CORR} , turbulent (P=1.5)
1	609	0.0846	0.2870	1.0160	0.675	0.1180	1.0704	0.6415	0.561	0.0968	0.0602	0.0693
2	----	-----	-----	-----	-----	-----	-----	-----	-----	-----	-----	-----
3	----	-----	-----	-----	-----	-----	-----	-----	-----	-----	-----	-----
4	----	-----	-----	-----	-----	-----	-----	-----	-----	-----	-----	-----
5	----	-----	-----	-----	-----	-----	-----	-----	-----	-----	-----	-----
6	1367	0.0846	0.1815	0.5580	0.0676	0.1182	1.1429	0.6971	0.738	0.2332	0.0701	0.1159
7	979	0.0847	0.2064	0.5875	0.0675	0.0590	1.1596	0.7070	0.597	0.2692	0.0933	0.1403
8	1043	0.0846	0.2146	0.5967	0.0676	0.1772	1.1291	0.6466	0.582	0.1770	0.0492	0.0827
9	1093	0.0845	0.2057	0.5867	0.0338	0.1181	1.1761	0.6999	0.560	0.2874	0.1096	0.1614
10	1143	0.0846	0.2108	0.5924	0.1013	0.1181	1.1163	0.6604	0.623	0.1677	0.0364	0.0677
11	1435	0.1824	0.1706	0.6486	0.0677	0.1182	1.1303	0.6629	0.626	0.1887	0.1402	0.1539
12	1494	0.1824	0.1677	0.6442	0.0338	0.0590	1.1527	0.7262	0.608	0.2785	0.2093	0.2309
13	1545	0.1828	0.1680	0.6446	0.1014	0.0590	1.0926	0.6767	0.655	0.1425	0.0969	0.1076
14	1645	0.1827	0.1717	0.6502	0.1014	0.1772	1.0705	0.6387	0.668	0.0960	0.0607	0.0684
15	1695	0.1823	0.1755	0.6559	0.0337	0.1769	1.1290	0.6648	0.600	0.1881	0.1409	0.1541
16	1746	0.1826	0.1724	0.6514	0.0675	0.1180	1.1113	0.6655	0.610	0.1637	0.1182	0.1303
17	----	-----	-----	-----	-----	-----	-----	-----	-----	-----	-----	-----
18	----	-----	-----	-----	-----	-----	-----	-----	-----	-----	-----	-----
19	----	-----	-----	-----	-----	-----	-----	-----	-----	-----	-----	-----
20	----	-----	-----	-----	-----	-----	-----	-----	-----	-----	-----	-----
21	----	-----	-----	-----	-----	-----	-----	-----	-----	-----	-----	-----
22	----	-----	-----	-----	-----	-----	-----	-----	-----	-----	-----	-----
23	1595	0.1827	0.1706	0.6485	0.0676	0.1181	1.1143	0.6681	0.631	0.1694	0.1233	0.1351
24	2068	0.1824	0.1360	0.3908	0.0338	0.1182	1.1917	0.6959	0.630	0.3067	0.1259	0.1759
25	2121	0.1827	0.1353	0.3900	0.1015	0.1182	1.1374	0.6682	0.685	0.2022	0.0600	0.0931
26	2328	0.1823	0.1358	0.3906	0.0676	0.0590	1.1887	0.7105	0.666	0.3196	0.1276	0.1759
27	2225	0.1824	0.1410	0.3965	0.0676	0.1772	1.1368	0.6409	0.633	0.1836	0.0570	0.0889

Appendix J

Experimental Data for Expansion Ratio = 0.8

Run number	Reading number	Parameters					Measured data			Derived data		
		τ	F_L	F_T	G_p	G_w	P_{hi}/P_{in}	P_{lo}/P_{in}	m , lb/sec	η , uncorrected	η_{CORR} , laminar ($f=0.8$)	η_{CORR} , turbulent ($f=1.4$)
1	600	0.0846	0.3144	1.0537	0.0624	0.1091	1.0567	0.6906	0.465	0.0929	0.0502	0.0591
2	----	-----	-----	-----	-----	-----	-----	-----	-----	-----	-----	-----
3	----	-----	-----	-----	-----	-----	-----	-----	-----	-----	-----	-----
4	----	-----	-----	-----	-----	-----	-----	-----	-----	-----	-----	-----
5	----	-----	-----	-----	-----	-----	-----	-----	-----	-----	-----	-----
6	1283	0.0846	0.2040	0.5847	0.0626	0.1093	1.1101	0.7416	0.610	0.2174	0.0453	0.0830
7	978	0.0847	0.2457	0.6299	0.0626	0.0547	1.1319	0.7523	0.499	0.2710	0.0625	0.1185
8	1042	0.0846	0.2552	0.6396	0.0626	0.1642	1.1073	0.6870	0.500	0.1706	0.0247	0.0630
9	1092	0.0845	0.2505	0.6348	0.0313	0.1095	1.1445	0.7394	0.467	0.2793	0.0759	0.1350
10	1179	0.0846	0.2457	0.6299	0.0938	0.1093	1.0895	0.7072	0.529	0.1544	0.0030	0.0394
11	1434	0.1824	0.1878	0.6740	0.0626	0.1094	1.1011	0.7050	0.523	0.1725	0.1177	0.1336
12	1493	0.1825	0.1889	0.6756	0.0312	0.0546	1.1160	0.7690	0.489	0.2587	0.1795	0.2056
13	1544	0.1828	0.1915	0.6793	0.0936	0.0545	1.0649	0.7224	0.553	0.1200	0.0673	0.0799
14	1644	0.1826	0.1885	0.6749	0.0936	0.1642	1.0469	0.6823	0.578	0.0748	0.0344	0.0429
15	1694	0.1823	0.1975	0.6876	0.0313	0.1639	1.0991	0.7073	0.504	0.1706	0.1168	0.1325
16	1745	0.1826	0.1919	0.6798	0.0626	0.1094	1.0847	0.7077	0.508	0.1468	0.0947	0.1086
17	----	-----	-----	-----	-----	-----	-----	-----	-----	-----	-----	-----
18	----	-----	-----	-----	-----	-----	-----	-----	-----	-----	-----	-----
19	----	-----	-----	-----	-----	-----	-----	-----	-----	-----	-----	-----
20	----	-----	-----	-----	-----	-----	-----	-----	-----	-----	-----	-----
21	----	-----	-----	-----	-----	-----	-----	-----	-----	-----	-----	-----
22	----	-----	-----	-----	-----	-----	-----	-----	-----	-----	-----	-----
23	1594	0.1827	0.1902	0.6775	0.0625	0.1093	1.0853	0.7100	0.529	0.1491	0.0965	0.1100
24	2104	0.1822	0.1621	0.4193	0.0313	0.1093	1.1488	0.7454	0.494	0.2948	0.0849	0.1433
25	2120	0.1827	0.1572	0.4142	0.0939	0.1094	1.1038	0.7162	0.579	0.1848	0.0226	0.0602
26	2327	0.1823	0.1584	0.4154	0.0627	0.0545	1.1458	0.7598	0.548	0.3084	0.0843	0.1409
27	2224	0.1824	0.1614	0.4185	0.0627	0.1643	1.1048	0.6879	0.545	0.1674	0.0242	0.0595

References

- Box, G.E.P.; and Behnken, D.W.: Some New Three Level Designs for the Study of Quantitative Variables. *Technomet*, vol. 2, no. 4, Nov. 1960, pp. 455–75.
- Emmert, H.D.: Current Design Practices for Gas-Turbine Power Elements. *Trans ASME*, vol. 72, no. 2, Feb. 1950, pp. 189–200.
- Foa, J.V.: *Elements of Flight Propulsion*. John Wiley and Sons, New York, NY, 1960, pp. 161–166.
- Fronek, D.L., et al.: A Distributed Data Acquisition System for Aeronautics Test Facilities. NASA TM-88961, 1987.
- Glawe, G.E., and Krause, L.N.: Miniature Probes for use in Gas Turbine Testing Component Reliability Measuring Instruments. NASA TM X-71638, 1974.
- Hoerler, H.U., Abschaetzung der Verluste in Instationaer-gasdynamischen Kanaltrommel-Drucktauschern. Doctoral Dissertation, Eidgenoessische Technische Hochschule, Zurich, Switzerland, 1969.
- Jenny, E., and Zumstein, B.: Pressure Wave Super-Charging of Passenger Car Diesel-Engines. Conference on Turbocharging and Turbochargers, The Institution of Mechanical Engineers, London, England, 1982, pp. 129–141.
- Keller, J.J.: Some Fundamentals of the Supercharger Complex Machinery for Direct Fluid-Fluid Energy Exchangers, J.F. Sladky Jr., ed. ASME AD-07, ASME, New York, NY, 1984, pp. 47–54.
- Kentfield, J.A.C.: The Performance of Pressure-Exchanger Dividers and Equalizers. *J. Basic Eng.*, *Trans. ASME*, Sept. 1969, pp. 361–370.
- Kentfield, J.A.C.: On the Feasibility of Gas-Turbine Pressure-Gain Combustors. *Int. J. Turbo Jet Eng.*, vol. 12, no. 1, 1995, pp. 29–36.
- Lieblein, S.: *Experimental Flow in Two-Dimensional Cascades*. Chapt. VI, NASA SP-36, 1965.
- Mattingly, J.D.; Heiser, W.H.; and Daley, D.H.: *Aircraft Engine Design*. AIAA, New York, 1987.
- Meyer, A.: Recent Developments in Gas Turbines. *Mech. Eng.*, vol. 69, no. 4, 1947, pp. 273–277.
- Paxson, D.E.: Comparison Between Numerically Modelled and Experimentally Measured Wave-Rotor Loss Mechanisms. *J. Propul. P.*, vol. 11, no. 5, 1995, pp. 908–914.
- Peacock, N.J.; and Sadler, J.H.R.: Advanced Propulsion Systems for Large Subsonic Transports. *J. Propul. P.*, vol. 8, no. 3, May-June 1992, pp. 703–708.
- Pearson, R.D.: A Gas Wave-Turbine Engine Which Developed 35 H.P., and Performed Over a 6:1 Speed Range. Proceedings of the 1985 ONR/NAVAIR Wave Rotor Research and Technology Workshop, R.P. Shreeve and A. Mathur, eds, Report NPS-67-85-008, Naval Postgraduate School, Monterey, CA, 1985, pp. 125–170.
- Roelke, R.J.: Miscellaneous Losses, Chapt. 8, *Turbine Design and Application*, NASA SP-290, vol. 2, 1994, pp. 125–148.
- Schlichting, H.: *Boundary-Layer Theory*. McGraw-Hill Book Company, New York, NY, 1979.
- Seshadri, S.; and Deming, S.N.: Box-B Interactive Computer Programs for Using Three- and Four-Factor Box-Behnken Designs in Research, Development, and Manufacturing (Version 2.1), [Computer Program]. Available Distributor: Statistical Programs, Houston, TX (Address: 9941 Rowlett, Suite 6, Zip 77075), 1990.
- Thayer, W.J. III, et al.: Energy Exchanger Performance and Power Cycle Evaluation: Experiments and Analysis. Final Report. 23 May 1978–31 Dec. 1980, Mathematical Sciences, Northwest, Inc., April 1981 (DE-AC06-78ER0-1084).
- Weatherston, R.C., et al.: Gasdynamics of a Wave Superheater Facility for Hypersonic Research and Development. CAL Report No. AD-118-A Comell Aeronautical Lab, Inc. Buffalo, NY, 1959.
- Weber, H.E.: *Shock Wave Engine Design*. John Wiley and Sons, Inc., New York, NY, 1995.
- Welch, G.E., and Chima, R.V.: Two-Dimensional CFD Modeling of Wave Rotor Flow Dynamics. NASA TM-106261, 1994.
- Welch, G.E.; Jones, S.M.; and Paxson, D.E.: Wave Rotor-Enhanced Gas Turbine Engines. *J. of Engineering for Gas Turbines and Power*, vol. 119, April 1997, pp. 469–477.
- Welch, G.E.: Two-Dimensional Computational Model for Wave Rotor Flow Dynamics. ASME paper 96-GT-550 (NASA TM-107192), 1996.
- Wilson, J.; and Paxson, D.E.: Wave Rotor Optimization for Gas Turbine Engine Cycles. *J. Propul. P.*, vol. 12, no. 4, July-Aug. 1996, pp. 778–785.
- Zauner, E., et al.: Gas Turbine Topping Stage Based on Energy Exchangers: Process and Performance. ASME Paper 93-GT-58, 1993.

REPORT DOCUMENTATION PAGE			Form Approved OMB No. 0704-0188	
Public reporting burden for this collection of information is estimated to average 1 hour per response, including the time for reviewing instructions, searching existing data sources, gathering and maintaining the data needed, and completing and reviewing the collection of information. Send comments regarding this burden estimate or any other aspect of this collection of information, including suggestions for reducing this burden, to Washington Headquarters Services, Directorate for Information Operations and Reports, 1215 Jefferson Davis Highway, Suite 1204, Arlington, VA 22202-4302, and to the Office of Management and Budget, Paperwork Reduction Project (0704-0188), Washington, DC 20503.				
1. AGENCY USE ONLY (Leave blank)		2. REPORT DATE August 1997	3. REPORT TYPE AND DATES COVERED Final Contractor Report	
4. TITLE AND SUBTITLE An Experiment on Losses in a Three-Port Wave Rotor			5. FUNDING NUMBERS WU-523-26-33 C-NAS3-27186	
6. AUTHOR(S) Jack Wilson				
7. PERFORMING ORGANIZATION NAME(S) AND ADDRESS(ES) NYMA Inc. 2001 Aerospace Parkway Brook Park, Ohio 44142			8. PERFORMING ORGANIZATION REPORT NUMBER E-10364	
9. SPONSORING/MONITORING AGENCY NAME(S) AND ADDRESS(ES) National Aeronautics and Space Administration Lewis Research Center Cleveland, Ohio 44135-3191			10. SPONSORING/MONITORING AGENCY REPORT NUMBER NASA CR-198508	
11. SUPPLEMENTARY NOTES Project Manager, Kestutis C. Civinskas, Propulsion Systems Division, NASA Lewis Research Center, organization code 2760, (216) 433-3944.				
12a. DISTRIBUTION/AVAILABILITY STATEMENT Unclassified - Unlimited Subject Category 07 This publication is available from the NASA Center for AeroSpace Information, (301) 621-0390.			12b. DISTRIBUTION CODE	
13. ABSTRACT (Maximum 200 words) Wave rotors used in a gas turbine topping cycle, offer a potential route to higher specific power and lower specific fuel consumption. In order to exploit this potential properly, it is necessary to have some realistic means of calculating wave rotor performance, taking losses into account, so that wave rotors can be designed for good performance. This, in turn, requires a knowledge of the loss mechanisms. The experiment reported here was designed as a statistical experiment to identify the losses due to finite passage opening time, boundary layers, and leakage. On analyzing the data, incidence loss was also determined to be an important loss. For simplicity, the experiment used a three-port, flow divider, wave cycle, but the results are applicable to other cycles. A 12-in.-diameter rotor was used with two different lengths, 9 and 18 in., and two different passage widths, 0.25 and 0.54 in., in order to vary the boundary layer thicknesses and the opening time. To vary leakage, moveable end walls were provided so that the rotor to end-wall gap could be adjusted. The experiment is described and the results are presented together with a parametric fit to the data. The fit shows that there will be an optimum passage width for a given wave rotor since, as the passage width increases, boundary layer losses decrease, but opening-time losses increase and vice-versa. Leakage losses can be made small at reasonable gap sizes. Inlet ports should be designed to minimize incidence losses.				
14. SUBJECT TERMS Wave rotor; Losses			15. NUMBER OF PAGES 44	
			16. PRICE CODE A03	
17. SECURITY CLASSIFICATION OF REPORT Unclassified	18. SECURITY CLASSIFICATION OF THIS PAGE Unclassified	19. SECURITY CLASSIFICATION OF ABSTRACT Unclassified	20. LIMITATION OF ABSTRACT	